Quarterly Journal of the Royal Meteorological Society Q. J. R. Meteorol. Soc. (2012)

The temporal cascade structure of reanalyses and global circulation models

J. Stolle,[a]* S. Lovejoy[a] and D. Schertzer[b]
[a] *Physics, McGill University, 3600 University St., Montreal, Que. H3A 2T8, Canada*
[b] *CEREVE, Université Paris Est, France*

*Correspondence to: J. Stolle and S. Lovejoy, Physics, McGill University, 3600 University St., Montreal, Que. H3A 2T8, Canada. E-mail: stollej@physics.mcgill.ca; lovejoy@physics.mcgill.ca

The spatial stochastic structure of deterministic models of the atmosphere has been shown recently to be well modelled by multiplicative cascade processes; in this paper we extend this to the time domain. Using data from the European Centre for Medium Range Weather Forecasting's (ECMWF) reanalyses (ERA40) and two meteorological models (Global Forecast System and Global Environmental Multiscale), we investigate the temporal cascade structures of the temperature, humidity and zonal wind at various altitudes, latitudes and forecast times. First, we estimate turbulent fluxes from the absolute second-order time differences, showing that the fluxes are generally very close to those estimated in space at the model dissipation scale; thus validating the flux estimates. We then show that temporal cascades with outer scales typically in the range 5–20 days can accurately account for the statistical properties over the range from 6 h up to 3–5 days. We quantify the (typically small) differences in the cascades from model to model, as functions of latitude, altitude and forecast time. By normalizing the moments by the theoretical predictions for universal multifractals, we investigate the 'Levy collapse' of the statistics somewhat beyond the outer cascade limit into the low-frequency weather regime. Although due to finite size effects and the small outer temporal scale, the temporal scaling range is narrow (12–24 h up to 2–10 days), we compare the spatial and temporal statistics by constructing space-time (Stommel) diagrams, finding space-time transformation velocities of 450–1000 km day^{-1}, comparable to those predicted based on the solar energy flux driving the system. This transition time-scale corresponding to planetary size structures objectively defines the transition from usual weather to a low-frequency weather regime with much lower variability. Finally, we discuss the implications for ensemble forecasting systems, stochastic parametrization and stochastic forecasting.

Key Words: turbulence; cascade; fractal; multifractal; circulation model; reanalysis

Received 25 January 2010; Revised 13 November 2011; Accepted 1 February 2012; Published online in Wiley Online Library

Citation: Stolle J, Lovejoy S, Schertzer D. 2012. The temporal cascade structure of reanalyses and global circulation models. *Q. J. R. Meteorol. Soc.* DOI:10.1002/qj.1916

1. Introduction

'Weather prediction by numerical process' (Richardson, 1922) is widely celebrated as the pioneering work laying the basis of modern numerical weather forecasting. In it, Richardson eschewed approximations and attempted a brute force numerical integration of the dynamical fluid equations. While these equations are deterministic, numerical weather prediction has been increasingly transformed into sophisticated ensemble forecast systems

(EFS). This modern incarnation of 'Richardson's dream' (Lynch, 2006) has the stochastic objectives of predicting the future states of the atmosphere as well as their probabilities of occurrence. Ensemble forecast systems involve stochastic subgrid parametrizations (Buizza *et al.*, 1999; Palmer, 2001; Palmer and Williams, 2010) and therefore require knowledge of the stochastic properties of the deterministic models.

Interestingly, Richardson is not only the father of numerical weather forecasting, he is also – thanks to his iconic poem describing cascades – considered to be the 'grandfather' of cascade approaches. Following the development of the classic turbulence laws of Richardson, Kolmogorov, Obhukhov, Corrsin and Bolgiano and starting in the 1960s, these have spawned explicit stochastic cascade models. Today these are well understood and are known to be the generic multifractal process. Multifractal intermittency has been reported widely in laboratory and small-scale atmospheric experiments from the mid-1980s onwards (see the review by Anselmet (2001)). Recently the deterministic and stochastic approaches have been shown to be surprisingly compatible. Stolle *et al.* (2009) analysed both meteorological reanalyses (European Centre for Medium range Weather Forecasting's (ECMWF) reanalysis (ERA40)) and meteorological forecasting models ((Global Forecast System (GFS) and Global Environmental Multiscale (GEM)) and showed that the spatial statistics of the turbulent fluxes associated with the temperature, zonal wind and humidity were indeed very close to those predicted by cascade models with deviations typically $< \pm 1\%$ over the range of 5000 km down to the model/reanalysis (hyper) viscous dissipation scales. Lovejoy and Schertzer (2011) found similar results for the ECMWF interim reanalysis products, extending these results to the geopotential height, to the vertical wind, and to the meridional wind fields as well as the corresponding turbulent fluxes. At the same time, the increasing availability of remote and *in situ* global-scale data has made it possible to directly confirm that these also have qualitatively and quantitatively very similar cascade structures up to planetary scales. The similitude of the global-scale data, models and reanalyses provides the basis for understanding atmospheric variability over huge spatial scales – see the reviews by Lovejoy and Schertzer (2010, 2012a). A wide-scale range of cascade processes is possible because it appears that the vertical structure of the atmosphere is scaling but with different exponents than in the horizontal structure. This implies that the cascades are anisotropic with structures becoming progressively flatter at larger and larger scales but in a scaling manner (Lovejoy *et al.*, 2007, 2009a). For a theoretical model based on the (fractional) vorticity equation, see Schertzer *et al.*(2012).

These model, reanalysis, *in situ* and remote-sensing studies have shown that the wind and other atmospheric fields are scaling over wide ranges (see Lovejoy *et al.* (2009b) for the reinterpretation of aircraft measurements of wind). The wind is critical because physically it advects the fields and dimensionally it connects space and time. This suggests that the fields should be scaling in time as well as in space. It even seems that the corresponding space–time relations can even be quite accurately deduced from first principles, and the argument (Lovejoy and Schertzer, 2010) goes as follows. Starting from the top of the atmosphere, there is roughly 1 kW m^{-2} of incident solar energy flux. Of this, about 200 W m^{-2} is absorbed by the Earth (Monin, 1972). If we distribute this over the troposphere (thickness $\approx 10^4$ m), with an air density $\approx 1\ \mathrm{kg\,m}^{-3}$, and assume a 2% conversion of energy into kinetic energy (Palmén, 1959; Monin, 1972), then we obtain a value $\varepsilon \approx 5\times10^{-4}\mathrm{m}^2\mathrm{s}^{-3}$, which is indeed the typical value measured in small-scale turbulence; see the review in Lovejoy and Schertzer (2010) – more modern data yield the global estimate $\varepsilon \approx 10^{-3}\ \mathrm{m}^2\mathrm{s}^{-3}$, although with some variation with altitude and latitude (note, $\mathrm{m}^2\mathrm{s}^{-3} = \mathrm{W\ kg}^{-1}$). If we now use the Kolmogorov relation $\Delta v(\Delta x) = \varepsilon^{1/3}\Delta x^{1/3}$ – which is apparently valid in the horizontal (but not vertical) up to near planetary scales – then we find that using $L_\mathrm{e} = \Delta x \approx 20\,000$ km, $\Delta v \approx 20\ \mathrm{m\,s}^{-1}$ and the corresponding lifetime of structures ('the eddy turn-over time') is $\tau_\mathrm{w} = L_\mathrm{e}^{2/3}\varepsilon^{-1/3} \approx 10$ days. While the predicted velocity difference is very close to the mean planetary antipodes differences ($17.3 \pm 5.7\ \mathrm{m\ s}^{-1}$), the lifetime is quite close to the transition from the weather regime to the low frequency weather regime ('spectral plateau') with much flatter spectra (Lovejoy and Schertzer, 1986). Figure 1 shows that for instrumental surface temperatures, the implied 'dimensional transition' does indeed occur near this scale. Similarly – although the data are much sparser – the ocean appears to have a global (near surface) energy flux $\varepsilon_\mathrm{o} \approx 10^{-8}\ \mathrm{m}^2\mathrm{s}^{-3}$, implying (again using L_e) a critical ocean time-scale $\tau_\mathrm{o} \approx 1$ yr, as confirmed in Figure 1 using sea-surface temperature (SST) measurements (this estimate is from ocean drifter data; see Lovejoy and Schertzer (2012a) for this and for a comprehensive review). For shorter scales, the spectra of 'ocean weather' sea-surface temperatures are very similar to atmospheric weather temperature spectra, whereas at longer time-scales they also display a marked flattening, a spectral plateau although with a larger (absolute) spectral exponent.

The upshot of this is that we expect the meteorological models and reanalyses to display a scaling cascade structure for high 'weather' frequencies, $\omega > \omega_\mathrm{w} = \tau_\mathrm{w}^{-1}$ and that this will break down at scales somewhere in the vicinity of 10 days. Whereas for the high weather frequencies, $E(\omega) \approx \omega^{-\beta_w}$ with generally $\beta_\mathrm{w} > 1$, in the 'low-frequency weather' regime ($\omega < \omega_\mathrm{w}$) we find a relatively flat 'spectral plateau' (Lovejoy and Schertzer, 1986) with $\beta_\mathrm{w} < 1$. However, the significance of the transition is best appreciated in real space by considering fluctuations Δf of an atmospheric field f. Since both the weather and the low frequency weather regimes are scaling we have $\Delta f \approx \Delta t^H$, and the transition is from $H > 0$ to $H < 0$ at ω_w. This implies that whereas in the weather regime fluctuations tend to grow with scale (Δt), in the low-frequency weather regime they tend to diminish with scale. Physically, the low-frequency weather regime is thus perceived to be 'stable'. In Lovejoy and Schertzer (2012b) it is argued that this stability can be exploited by averaging over the entire low-frequency weather regime (out to a transition to the climate regime at $\omega_\mathrm{c} \approx (10\ \mathrm{yr})^{-1}$ to $(30\ \mathrm{yr})^{-1}$, where H is again > 0) to define a climate 'state'; the even lower frequency variations in this state corresponds to our notions of 'climate change'.

Although this paper focuses on the weather regime, it is necessary to make a few more comments on the weather, low-frequency weather and the transition between the two. Since many atmospheric processes have weather spectral exponents β_w near the value 2, and since the corresponding β_lw is small, the Ornstein–Uhlenbeck (OU) spectrum $E(\omega) \propto (\omega^2 + \omega_0^2)^{-1}$ (i.e. with $\beta_\mathrm{w} = 2$, $\beta_\mathrm{lw} = 0$ and transition at ω_0) is approximately valid. An OU

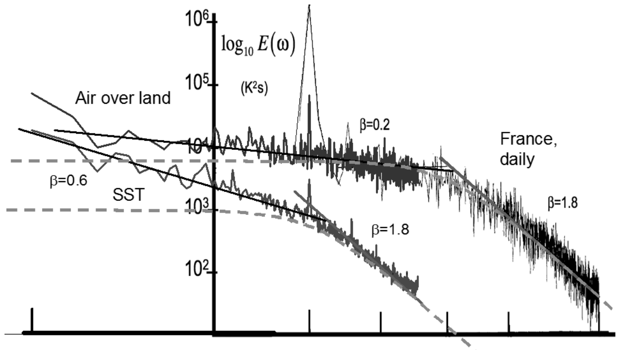

Figure 1. This figure superposes the ocean and atmospheric spectral plateaus showing their great similarity. (Left) A comparison of the monthly sea-surface temperatures (SST) spectrum (bottom, blue) and monthly atmospheric temperatures over land (top, purple) for monthly temperature series from 1911 to 2010 on a 5° × 5° grid; from NOAA NCDC data (Smith *et al.*, 2008). Only near-complete series (missing less than 20 months out of 1200) were considered: 465 for the SST, 319 for the land series; missing data were filled using interpolation. The reference slopes correspond to spectra of the form $E(\omega) \approx \omega^{-\beta}$ with $\beta = 0.2$ (top), 0.6 (bottom left) and 1.8 (bottom right). A transition at 1 yr corresponds to a mean ocean $\varepsilon_o \approx 1 \times 10^{-8}\mathrm{m}^2\mathrm{s}^{-3}$. Note the apparent beginning of a low-frequency rise at around $(30\ \mathrm{yr})^{-1}$. (Right) The average of five spectra from a sections 6 yr long of a 30 yr series from daily temperatures at a station in France (black, top, taken from Lovejoy and Schertzer (1986)). The red reference line has a slope 1.8 (there is also a faint slope 0 reference line). The relative up–down placement of this daily spectrum with the monthly spectra (corresponding to a constant factor) was determined by aligning the atmospheric spectral plateaus (i.e. the top right black and top left purple spectra). We have included common Ornstein–Uhlenbeck (OU) process fits (orange dashed lines) to each of the datasets to demonstrate that this common fit does not agree with the trends in the data. This figure is available in colour online at wileyonlinelibrary.com/journal/qj

process is precisely a Gaussian process with this spectrum and it corresponds to white noise smoothed over frequencies $> \omega_0$. Multivariate OU processes are used as the basis for stochastic linear modelling approaches for scales up to ≈ 1 yr, see for example Penland (1996).

As a model, there are two shortcomings of OU processes: (i) neither high- nor low-frequency exponents have quite the right values (implying that there are long-range statistical dependencies); (ii) that it neglects the strong (non-Gaussian) intermittency in the weather regime (discussed below). In Figure 1 we compare the atmospheric and SST spectra with OU spectra fit to the high-frequency parts of the spectrum and we see that it is not perfectly flat, but that $\beta_{\mathrm{lw}} \approx 0.2$ for the atmospheric temperature and $\beta_{\mathrm{lo}} \approx 0.6$ for the SST spectra ('*lo*' for 'low frequency ocean'). There are now many studies estimating β_{lw} and β_{lo}, most of which find β_{lw} in the range 0.2 to 0.4 (Koscielny-Bunde *et al.*, 1998; Fraedrich and Blender, 2003; Bunde *et al.*, 2004; see Eichner *et al.* 2003; Huybers and Curry, 2006) and for sea-surface temperatures $\beta_{\mathrm{lo}} \approx 0.6$ (Monetti *et al.*, 2003; Huybers and Curry, 2006); this issue is reviewed in Lovejoy and Schertzer (2012b) where it is also argued on the basis of generalizations of cascade processes that these exponents are theoretically expected.

In the following, although we do compare our results to the predictions of OU processes, of necessity they will not be too different from the model analyses. This is because the corresponding model and reanalysis outputs are available only every 6 h at best – and for many (especially near-surface) fields there is a technical analysis difficulty due to the diurnal cycle – so that the scaling range up to τ_{w} (in the range 5–20 days) is quite limited. Nevertheless in this paper we attempt to quantitatively characterize it and compare it with the corresponding spatial cascades and to intercompare the various products.

This paper is structured as follows. In section 2 we present the numerical outputs, which we analyse, and we explain the technique for estimating the fluxes in both space and in time, touching on other relevant cascade studies. In sections 3 and 4 we recapitulate pertinent spatial cascade results from Stolle *et al.* (2009) and we then systematically examine the temporal cascade structure for the different fields (horizontal wind, temperature, humidity), different models and as functions of altitude. In section 5 we compare the statistics of the fluxes estimated in the spatial domain at the dissipation scale with those estimated in the temporal domain in the scaling regime. We then discuss space–time ('Stommel') diagrams and show how to empirically construct them from the outputs using the spatial and temporal scale-by-scale flux statistics. We comment on the large space limit and the transition from weather to climate. Finally in section 6 we conclude.

2. Multiplicative cascades, turbulent fluxes and analysis techniques

2.1. *Multiplicative cascades*

2.1.1. *Spatial cascades*

During the 1960s and early 1970s, intermittency was increasingly acknowledged as an important phenomenon, but its effect was usually considered small, leading primarily to small 'intermittency corrections' to the spectral exponents. The main statistical models (such as those used in statistical closures) assumed non-intermittent 'quasi-Gaussian statistics'. The Gaussian model leading to the classic Kolmogorov law $\Delta v = \varepsilon^{1/3}\Delta x^{1/3}$ (for velocity fluctuations Δv over distances Δx) is obtained by taking a Gaussian white noise energy flux ε and giving $\varepsilon^{1/3}$ a (fractional) integration of order 1/3 (i.e. a power law filter of order −1/3); the resulting v is a 'fractional Brownian motion'.

In order to take into account intermittency, it suffices to replace the Gaussian ε by the result of a multiplicative cascade; this is the fractionally integrated flux model (Schertzer and Lovejoy, 1987). In multiplicative cascades, large structures are broken up into smaller daughter structures that multiplicatively modulate the flux; this process is repeated to smaller and smaller scales (see Figure 2 for a schematic). Normalized cascade processes generally lead to multifractal fields with statistics:

$$\langle \varphi_\lambda^q \rangle = \lambda^{K(q)};\ \lambda = L/l, \tag{1a}$$

where '< . >' indicates ensemble (statistical) averaging, φ is the turbulent flux (e.g. the energy flux ε) normalized such that $<\varphi_\lambda>= 1$, $K(q)$ is a convex function describing the scaling behaviour of the q^{th} moment, λ is the ratio of the (large) scale L where the cascade starts to the scale of observation l. Note that in the quasi-Gaussian (non-intermittent) classic model we have the trivial $K(q) = 0$.

2.1.2. *Universality classes*

Since the cascade is multiplicative, its logarithm, the 'generator' is additive. It is therefore not surprising that – due

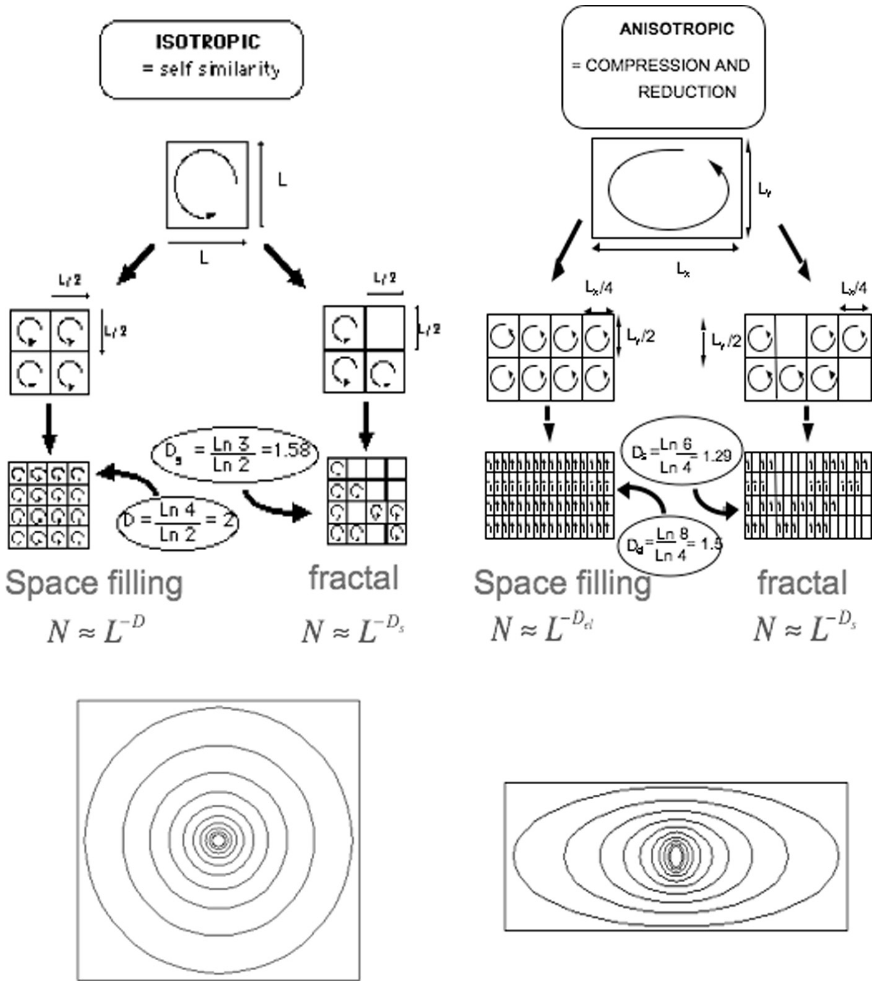

Figure 2. The left of the figure shows a schematic of an isotropic cascade. Due to nonlinear interactions with other eddies or to instability, a large eddy/structure (indicated as a square) breaks up into daughter eddies (smaller squares). Following the left-most arrow the energy flux is redistributed uniformly in space, the result is a homogeneous (non-fractal) cascade. Following the right-hand arrow, at each cascade step, we randomly allow one eddy in four to be 'dead', and the result is that turbulence is only active on a fractal set. At the bottom, we see the average shape as a function of scale of more realistic (isotropic eddies). The right-hand column is the same except that it shows an anisotropic cascade, a model of a vertical cross-section of the atmosphere (on the left a homogeneous, on the right, inhomogeneous, fractal model). The degree of stratification is characterized by an elliptical dimension $D_{\mathrm{el}} = 1.5$ in the example. (From Lovejoy and Schertzer (2010), adapted from Schertzer and Lovejoy (1987)). This figure is available in colour online at wileyonlinelibrary.com/journal/qj

to the additive central limit theorem for the sums of identical independently distributed random variables – there are specific (stable, attractive) 'universal' forms for the exponent $K(q)$:

$$K(q) = \frac{C_1}{(\alpha - 1)}(q^{\alpha} - q), \qquad (1b)$$

where $0 \le C_1 \le d$ is the 'co-dimension of the mean', which characterizes the sparseness of the set that gives the dominant contribution to the first-order statistical moment (the mean), and d is the dimension of the space over which the cascade is observed (Schertzer and Lovejoy, 1987). The multifractal index $0 \le \alpha \le 2$ characterizes the degree of multifractality, i.e. the shape of the $K(q)$ function. It is also the Levy index of the generator. If the cascade is uni-/monofractal, then $\alpha = 0$ whereas $\alpha = 2$ corresponds to the 'log-normal' multifractal. A 'universal multifractal' is the basin of attraction for a wide variety of different multiplicative processes. In our analyses, we will see that the universal form (Eq. (1b)) fits the empirical $K(q)$ quite well so that irrespective of whether the numerical models are indeed universal multifractals, the parameters C_1 and α give very convenient parametrizations of their forms and characterize the sparseness near the mean (C_1) and the curvature (and hence multifractality) near the mean (α). In this paper we therefore often use C_1 and α to reduce the characterization of the scaling (via the exponents $K(q)$) to manageable proportions. In any event, we show that over significant ranges of scale, the data display 'Levy collapses' when the moments are normalized by the theoretical universal $K(q)$, and this even for scales somewhat outside the scaling range (see Stolle *et al.* (2009) and section 5 below). In other words, the universality relation Eq. (1b) may be respected even when the scaling relation (1a) is not.

2.1.3. *Space–time cascades, causality*

If the velocity field is scaling in space, we expect the entire model to be scaling in space–time – at least up to time-scales corresponding to the external (planetary) scale. This is because physically the wind transports the fields and dimensionally it connects space and time. However, it is not enough to simply relabel one of the axes in Figure 2 as a time rather than as a space axis, even if we make the cascade anisotropic by differentially stratifying it (the right-hand side of Figure 2). The problem is that these pedagogical discrete in scale cascades are fundamentally left–right symmetric, and hence the result of merely relabelling a spatial axis as 'time' would be acausal. However, it turns out to be fairly straightforward to make causal space–time cascades (Marsan *et al.*, 1996), but the corresponding processes involve causal fractional integrations and cannot be illustrated as conveniently. The data analyses that follow are valid irrespective of the causal nature of the data: we will confine ourselves to pure temporal analyses (treating each pixel as a separate series), we will have the same formula as Eq. (1a) except that $\lambda = \tau_{\mathrm{ref}}/\tau$ where τ is the time-scale over which the flux is estimated and τ_{ref} a convenient reference outer time-scale, taken here as the total length of the time series.

2.2. *Estimating the turbulent fluxes*

In order to test Eq. (1a) we must therefore use an approach that does not require *a priori* assumptions about the physical nature of the relevant fluxes nor of their scale symmetries (isotropic or otherwise). If atmospheric dynamics are controlled by scale-invariant turbulent cascades of various (scale by scale) conserved fluxes φ then in a scaling regime the fluctuations $\Delta f(\Delta t)$ in an observable $f(t)$ (e.g. wind, temperature or radiance, t is time) over a duration Δt are related to the turbulent fluxes by a relation of the form $\Delta f(\Delta t) = \varphi \Delta t^H$ (this is a generalization of the Kolmogorov law for velocity fluctuations – for temporal fluctuations in a Lagrangian frame, $H = 1/2$, and $\varphi = \varepsilon^\eta, \eta = \frac{1}{2}$ and for spatial fluctuations we have $H = 1/3$ and $\varphi = \varepsilon^\eta, \eta = 1/3$). Without knowing η or H – or even the physical nature of the flux – we can use this to estimate the normalized (non-dimensional) flux φ' at the smallest resolution of our data:

$$\varphi' = \varphi/\langle\varphi\rangle = \Delta f/\langle\Delta f\rangle. \tag{2}$$

Note that if the fluxes are realizations of pure multiplicative cascades then the normalized η powers, $\varepsilon^\eta/\langle\varepsilon^\eta\rangle$, are also pure multiplicative cascades, so that $\varphi' = \varepsilon^\eta/\langle\varepsilon^\eta\rangle$ is a normalized cascade quantity.

The fluctuation $\Delta f(\Delta t)$ can be estimated in various ways; the simplest way is to use either absolute first or second differences (respectively $\Delta f(\Delta t) = |f(t+\Delta t) - f(t)|$ or $\Delta f(\Delta t) = |f(t) - (f(t+\Delta t) + f(t-\Delta t))/2|$) with Δt the smallest reliable resolution (we assume statistical translational invariance, no t dependence). These 'poor man's wavelets' are usually adequate – when as is typically the case, $0 \le H \le 1$ (first) or $0 \le H \le 2$ (second) differences are used. Alternatively other definitions of fluctuations (other wavelets) could be used. In the temporal analyses used here, we utilized absolute second differences, which are the same order of differences as the finite difference Laplacian used in the spatial analyses (Stolle *et al.* (2009), see also below). In section 5.1 we compare the temporal scaling of the two fluxes. Taking $\Delta t = \tau_{\mathrm{i}}$ as the smallest available time-scale and $\Lambda = t_{\mathrm{ref}}/\tau_{\mathrm{i}}$ as the corresponding ratio this yields: $\Delta f_\Lambda = |f(t) - (f(t+\tau_i) + f(x-\tau_i))/2|)$. The resulting high-resolution normalized flux estimates $\varphi_\Lambda = \Delta f_\Lambda/\langle\Delta f_\Lambda\rangle$ can then be degraded (coarse-grained by averaging) to a lower resolution $\tau > \tau_i$ scale ratio $\lambda = \tau_{\mathrm{ref}}/\tau < \Lambda$.

As empirical data are nearly always sampled at scales much larger than the dissipation scales, the scaling-range-based technique described above has wide applicability. In numerical models, however, where we have data down to the dissipation range, we find that the approach still works, but that the interpretation can be a little different. To see this, consider the example of the energy flux, $\varepsilon = \partial v^2/\partial t$. Taking the scalar product of the velocity equation with velocity $\underline{v}$ and recalling that at the dissipation scale the nonlinear terms are negligible, we obtain:

$$\varepsilon = \partial v^2/\partial t \approx \nu \underline{v} \cdot \nabla^2 \underline{v}, \tag{3}$$

where ν is the viscosity.

Considering the spatial dependence, standard manipulations (Landau and Lifschitz, 1959) give:

$$\varepsilon \approx \nu \left(\frac{\partial v_i}{\partial x_j} + \frac{\partial v_j}{\partial x_i}\right)^2 \approx \nu \left(\frac{\Delta v}{\Delta x}\right)^2, \tag{4}$$

(summing over the component indices $i, j = 1{,}3$) so that if Δx is in the dissipation range (e.g. the finest resolution of the model) then

$$\Delta v \approx \left(\frac{\varepsilon}{\nu}\right)^{1/2} \Delta x. \tag{5}$$

The models actually use hyperviscosities, which have the advantage of confining the dissipation to a small range of scales (about a factor of three). This means that their dissipation is due to a Laplacian raised to the power h (typically h is either 2 or 3), this is discussed in Stolle *et al.* (2009); they still lead to $\Delta v \propto \varepsilon^{1/2}$, i.e. to $\varphi' = \varepsilon^\eta/\langle\varepsilon^\eta\rangle$ with $\eta = 1/2$. We therefore see that the spatial scaling in Eq. (5) – which is only valid for Δx in the dissipation range of the model – leads to the dissipation range estimate $\varphi' = \varepsilon^\eta/\langle\varepsilon^\eta\rangle$ with $\eta = \frac{1}{2}$, whereas the corresponding scaling range (i.e. the Kolmogorov law, essentially dimensional analysis but without the viscosity ν) leads to the scaling regime formula $\Delta v \approx \varepsilon^{1/3}\Delta x^{1/3}$, i.e. to $\eta = 1/3$. In Stolle *et al.* (2009) we show how to relate the statistics of the dissipation range normalized flux $\varphi' = \varepsilon^{1/2}/\langle\varepsilon^{1/2}\rangle$ to the statistics of the scaling range normalized flux, $\varphi' = \varepsilon^{1/3}/\langle\varepsilon^{1/3}\rangle$.

Consider now the temporal fluctuations at the dissipation scale. We see that since $\varepsilon = \partial v^2/\partial t$, the relation between Δv, Δt and ε must be of the form $\varepsilon = (\Delta v)^2/\Delta t$, so that we obtain:

$$\Delta v \approx \varepsilon^{1/2}\Delta t^{1/2}. \tag{6}$$

Hence once again we have $\varphi' = \varepsilon^{1/2}/\langle\varepsilon\rangle^{1/2} = \Delta v/\langle\Delta v\rangle$, i.e. $\eta = 1/2$; the same as the spatial dissipation range exponent. Interestingly, unlike the spatial case where the dissipation scale $\Delta v(\Delta x)$ depends on the viscosity as well as ε, in time $\Delta v(\Delta t)$ does not explicitly involve ν and the dissipation scale relation Eq. (6) is actually the same as the classic Lagrangian relation, which holds for Δt in the scaling regime (Inoue, 1951; Landau and Lifschitz, 1959). Alternatively, with a large-scale space–time transformation velocity V_{trans}, we can take $\Delta x = V_{\mathrm{trans}}\Delta t$ and use the Kolmogorov formula in space to obtain $\eta = 1/3$ – see the discussion in section 5.2.

In the data analysis performed below we did not estimate $\Delta v(\Delta t)$ at the (model) temporal dissipation scale, which is of the order of the integration time step (τ_{st}) (see Table 1), instead the fluctuations were available only at the much longer scaling range Δt of 6 or 12 h (ERA40, GFS or GEM, respectively, see Table 1). The only caveat is that there is a (non-scaling) diurnal cycle that mostly affects the temperature at the 1000 mb level; this can lead to poor flux estimates. This can be avoided either by taking the analysis inner scale $\tau_i = 24$ h (at the price of losing some temporal resolution) or by detrending the fields by subtracting the time-averaged value at each time for each longitude and latitude as was done in this work.

The fact that the spatial and the temporal analyses both involve the fluxes $\varphi' = \varepsilon^{\eta}/\langle\varepsilon\rangle^{\eta}$; $\eta = 1/2$, shows that we are analysing the same physical quantity: in one case degrading it in the spatial domain, and in the other case the temporal domain. In addition, if space–time is roughly isotropic, then when they are systematically degraded in resolution in either space or in time we expect to find a single linear space–time relation between them. In actual fact, the models do not satisfy all the assumptions of these classic turbulence arguments so that in section 5.1 we check the relations between the Laplacian spatial estimated fluxes and those estimated by second-order temporal differences. However, we find that the ratio of the empirical spatial and temporal exponents η_x/η_t is indeed close to unity.

It turns out that if we extend these arguments to passive scalars (which can be used as simplified models of temperature and humidity) we obtain similar conclusions about the nature of the spatial versus temporal fluxes estimated from fluctuations (see also Stolle *et al.* (2009) for the more complex spatial scaling regime). Denoting by ρ the density of the passive scalar, and $\chi = \partial\rho^2/\partial t$ its variance flux, the dissipation range formula analogous to Eq. (3) is $\chi \approx \rho\kappa\nabla^2\rho$ (κ is the molecular diffusivity) leading to $\Delta\rho \approx (\chi/\kappa)^{1/2}\Delta x$, whereas the corresponding dissipation range temporal formula is $\Delta\rho \approx \chi^{1/2}\Delta t^{1/2}$, which as for velocity has the same $\chi^{1/2}$ behaviour ($\eta = 1/2$) in both space and in time – the temporal relation also being valid in the scaling regime (at least for Lagragian frames). For non-Lagrangian frames we again have to use $\Delta x = V_{\mathrm{trans}}\Delta t$, which yields $\eta = 1/3$.

2.3. *The outer scales*

A final practical consideration is that in the analyses, the outer scale is not known *a priori*, but is an empirically estimated parameter. It is therefore convenient to define a reference scale to non-dimensionalize the fluxes. With this convention, the basic prediction Eq. (1a) of multiplicative cascades is that the normalized moments $M_q = \langle\varphi_\lambda^q\rangle/\langle\varphi_1\rangle^q$ are expected to obey the generic multiscaling relation:

$$M_q = \left(\frac{\lambda}{\lambda_{\mathrm{eff}}}\right)^{K(q)}; \; \lambda = \tau_{\mathrm{ref}}/\tau; \lambda_{\mathrm{eff}} = \tau_{\mathrm{ref}}/\tau_{\mathrm{eff}}, \qquad (7)$$

where '< . >' indicates statistical (ensemble) averaging, τ is the temporal resolution of the flux and τ_{ref} is taken as the duration of the entire data set – or if space–time is quasi-isotropic so that the effective space–time transformation depends only on a 'transformation' velocity V_{trans} that is known (see section 5.2), we could use $\tau_{\mathrm{ref}} = L_{\mathrm{ref}}/V_{\mathrm{trans}}$. Finally, τ_{eff} is the effective outer temporal scale of the cascade (see section 4.1 and Figure 7 for estimates). The scale ratio $\lambda/\lambda_{\mathrm{eff}}$ is the overall ratio from the scale where the cascade started to the resolution scale τ.

Before demonstrating this on the reanalysis and model outputs, which have lower temporal resolutions and hence very short scaling ranges, we would like to present convincing evidence that the predictions of the cascade models are indeed accurately followed by real meteorological fields. Figure 3(a) shows the temporal analysis of hourly infrared imagery from the MTSAT geostationary satellite. The flux was estimated using the finite difference Laplacian at a 30 km spatial resolution and then degraded in time over 1440 images (about 2 months). From about an 1 h to about 2 days the evidence of converging straight lines (as predicted in Eq. (7)) is quite convincing (the corresponding spectrum starts to flatten at around 4 days), and it can be seen that the lines converge at somewhat larger scales ($\approx$ 48 days). Similarly, Figure 3(b) shows the analysis of 29 yr of hourly gridded rain-gauge data over the continental USA (details in Lovejoy and Schertzer (2010)); as can be seen, the outer scale is somewhat longer (42 days) but the deviations from scaling become important after about 7 days; notice that as expected, the intermitency is much higher for precipitation ($C_1 \approx$ 0.37 compared with $\approx$ 0.073 for the radiances in Figure 3(a)). These figures demonstrate the challenge we face with even lower temporal resolution data: the lifetime of planetary scale structures may be $\approx$ 5–10 days but the transition is not sharp so that the scaling of the moments of the fluxes is affected on scales as short as 2 days. That the outputs do indeed display cascade structures is shown in Figure 3(c), which is a typical spatial analysis; deviations are $< 1\%$ for scales < 5000 km.

Qualitatively, we can see that all the statistical moments have the same type of behaviour as a function of resolution $\lambda = \tau_{\mathrm{ref}}/\tau$. In particular, starting at the small scale (large λ, far right) part of the graphs and moving to longer time-scales, lower temporal resolutions (smaller λ, to the left), we notice that the moments initially respect power laws–at least approximately–emanating from a point. As q increases, the estimates are dominated by a smaller set of extreme values, eventually becoming spurious ('multifractal phase transitions'); the results for the larger q values were therefore not given. This is the prediction of multiplicative cascades in the time domain, Eqs. (1a and 7), the point marks the effective outer scale at which the cascade starts ($\lambda = \lambda_{\mathrm{eff}}$). At larger scales (typically greater than a week or so, the statistics 'flatten' out; below we argue that this corresponds to a transition from the weather to the low frequency weather regime.

Before continuing, let us return briefly to the Ornstein–Uhlenbeck processes that we discussed earlier. This will be a useful comparison point for our analyses. If we use the method outlined here to analyse an OU process, treating it as an unknown data field, the first step is to estimate the flux by taking the absolute second differences. Since the OU process is essentially a summed Gaussian white noise, this 'flux' will be a quasi-Gaussian process (essentially independent of the transition frequency ω_0) and by the central limit theorem, as we degrade the fluxes in order to estimate the moments at lower and lower resolutions, we expect rapid convergence to a flat ($K(q) = 0$) regime. Finally, since the flux is normalized by dividing by its ensemble average, the overall result is a 'universal' set of moments valid for any quasi-Gaussian process (at least with $\beta < 4$, the limit is a consequence of the second differencing used to estimate the

Table 1. Comparison of various model parameters. The time step is the model integration time step, the 'grid speed' is the ratio of finest model resolution to the time step. The time interval, T_i, is the smallest Δt used in the analyses, the 'analysis speed' is the ratio of the analysis spatial and temporal resolutions. For GFS, ERA40 the analyses were at 6 h. The 'typical transformation speed', V_{trans}, is the mean speed obtained from the space–time analyses of section 5.2 for all datasets at 700 mb.

Parameters	GEM	GFS	ERA 40
Time step (min) τ_{st}	22.5	7.5	30
Number of realizations in sample	505	1340	4384
Analysis time interval (h) τ_i	12	6, 24	6, 24
Assimilation cycle (h)	12	6	6
External time-scale of the data set τ_{ref}	223 days	300 days	1000 days
Model spatial resolution, L_g	$0.25^\circ \times 0.3^\circ$	$(0.47)^\circ \times (0.47)^\circ$	$(1.125)^\circ \times (1.125)^\circ$
Grid Speed (m s^{-1}), $V_{st} = L_i/\tau_{st}$	20.5	116.	69.
Number of vertical levels	28	64	60
Spatial resolution of analysis L_i	$0.6^\circ \times 0.6^\circ$	$1^\circ \times 1^\circ$	$1^\circ \times 1^\circ$
Analysis speed (m s^{-1})$V_i = L_i/\tau_i$	0.77	1.3	1.3
Typical space–time transformation speed (700 mb) V_{trans}	500 km day = 5.8 m s^{-1}	450 km day = 5.2 m s^{-1}	1000 km day = 11.6 m s^{-1}

flux). In Figure 3(d), we show these 'universal' moments up to order 2.9 obtained from 100 realizations of an OU process 2^{13} points long with $\omega_0 = (128)^{-1}$ (grid points)$^{-1}$. As expected, the result was essentially identical to that of a pure Gaussian white noise. The basic characteristics of the graph that will be useful when comparing with the corresponding model output analyses are: (i) the maximum $\log_{10}M \approx 0.46$ ($q = 2.9$; the corresponding value for $q = 2$ is $\log_{10}M \approx 0.20$); (ii) the outer scale is approximately a factor of 10 larger than the inner scale; (iii) the curves start to deviate significantly from the lines at scales larger than about five grid points; (iv) at scales of a factor of 100 grid points $\log_{10}M$ is already < 0.01; (v) the best fit corresponding universal multifractal parameters are $C_1 \approx 0.082$ and $\alpha \approx 1.79$.

It might be thought that because the C_1 values are typically 'small', the multifractal cascade effects are also small, however, this is not the case. For example, if $C_1 = 0.05$ for the wind (roughly the value estimated from aircraft, e.g. Lovejoy *et al.* (2010)), then for the energy flux $\varepsilon \approx \Delta v^3/\Delta x$ we have $C_1 = 0.05 \times 3^\alpha \approx 0.36$ (using $\alpha = 1.8$) so that the dominant contribution to the mean energy flux is from a fractal set with co-dimension 0.36. Taking the dissipation scale as $\approx$ 1 mm and the outer scale as 10^4 km, this implies $\lambda = 10^{10}$, so that the set giving the dominant contribution is of fraction $\lambda^{-C_1} \approx 10^{-4}$, so that 99.99% of the field is too weak to significantly contribute. Similarly, we can easily estimate that the variance (the $q = 2$ moment of ε) is determined by the extremes corresponding to a fraction (probabilities) of 10^{-13}; for quasi-Gaussian processes this would be closer to 10^{-1}. The point is that the variability builds up scale by scale and a 'low' exponent simply means that this happens 'slowly' with scale, yet the resulting variability may be enormous!

3. The model products

3.1. *The models*

3.1.1. *The Canadian Meteorological Centre Global Environmental Multiscale model)*

We chose two forecast models and one reanalysis, all recognized as being state-of-the-art: the Canadian Meteorological Centre (CMC) Global Environmental Multiscale (GEM), the NOAA Global Forecast System (GFS) model and the European Centre for Medium Range Weather Forecasting's (ECMWF) reanalysis (ERA40): see Table 1 for a summary of model and dataset characteristics. For all three products we analysed the three most dynamically significant fields: temperature (T), east–west (u) wind fields and specific humidity (h_s; GEM, ERA40) and relative humidity (h_r, GFS). For each, we investigated the cascade structure as a function of altitude, latitude and (for GEM, GFS) forecast horizon.

The GEM model is on a $0.25^\circ \times 0.3^\circ$ horizontal grid with 28 levels and our analysis used a $0.6^\circ \times 0.6^\circ$ resolution product (about 66 km resolution, the high-resolution GRIB dataset (CMC, 2009a) at five pressure levels (1000, 850, 700, 500 and 200 mb). We used 505 realizations taken from 20 September 2007 to 2 June 2008, which are initialized at either 1200 UTC or 0000 UTC, and analysed the initial objective analyses and the 48 h forecasts. In order to partially compensate for the smaller number of realizations and smaller spatial scale, τ_i was taken as 12 h. A 4DVAR 6 h assimilation is now used (CMC, 2009b). The model can be adapted, see Côté *et al.* (1998a, 1998b) for more details.

3.1.2. *The NOAA Global Forecast System model*

Like the CMC GEM model, the GFS is a global NWP model, which we analysed at its analysis ($t = 0$) and 48 h forecast ($t = 48$ h). The GFS model uses T254 Spectral and 768×384 Gaussian grids on 64 vertical levels. The data are obtained at a $1^\circ \times 1^\circ$ resolution at five pressure levels (1000, 850, 700, 500 and 200 mb) every 6 h; each initialization starts at 0000 UTC, 0600 UTC, 1200 UTC or 1800 UTC. The data were taken from 1 August 2007 to 30 June 2008 (with the exception of 700 mb u for which the first 61 days were corrupted). A total of 1340 realizations were analysed. When needed, due to the diurnal variation, fields were averaged over four consecutive periods so that T_i = either 6 or 24 h. The assimilation system used is 3DVAR (Okamoto and Derber, 2006) with an assimilation cycle of 6 h. For more information, see Sela (1982, 1988) and NCEP (2003).

3.1.3. *The European Centre for Medium Range Weather Forecasting's reanalysis product*

A reanalysis combines a model forecast with observational data using sophisticated data assimilation techniques, here a 6 h 3DVAR assimilation cycle was used. The product was made as uniform as possible over the 45 yr period

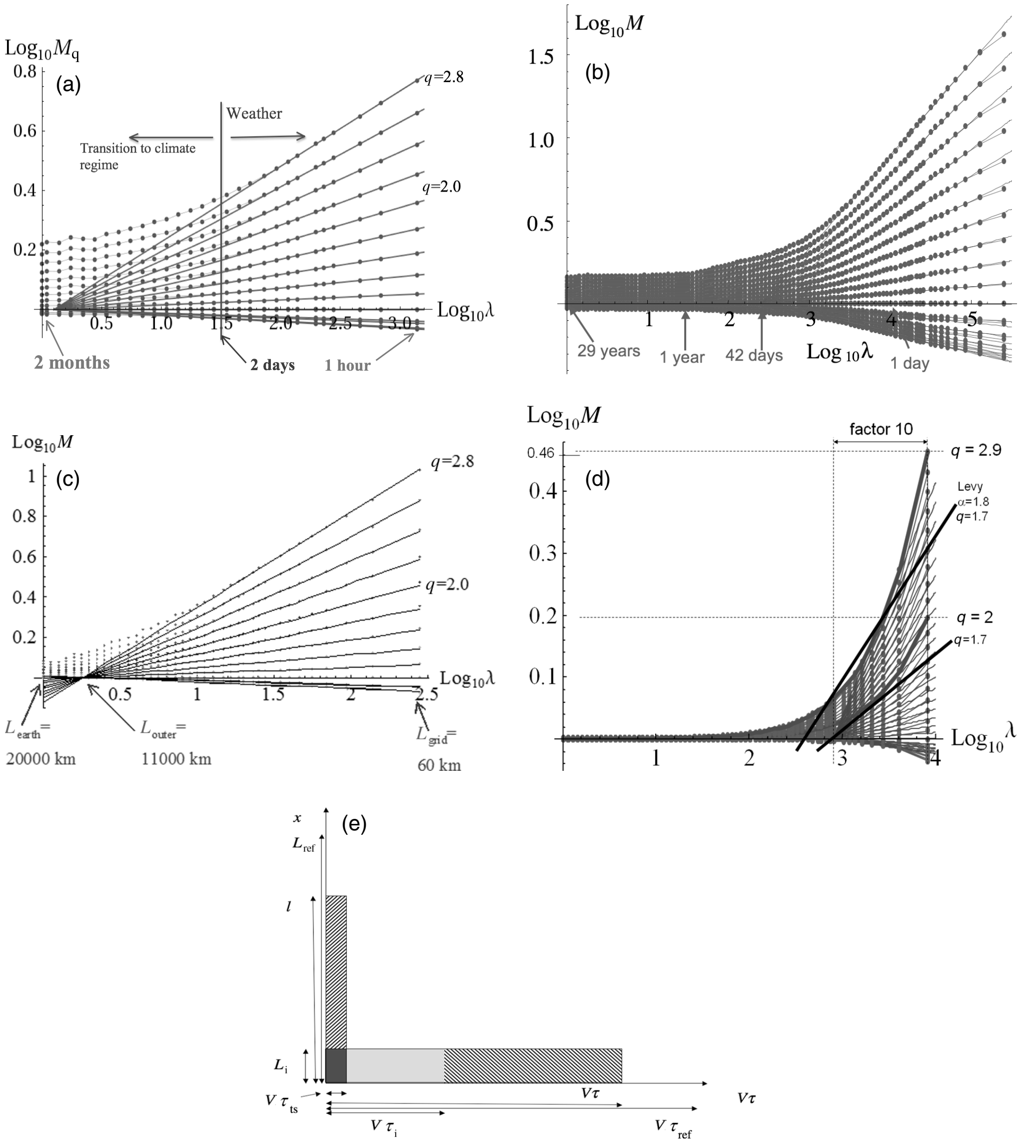

Figure 3. (a) Analysis of MTSAT hourly resolution thermal infrared (IR) imagery over the Pacific. The temporal analysis is of the spatial Laplacian (at 30 km resolution) geostationary MSTAT thermal IR imagery over the Pacific for two months. The external scale is 48 days, the multifractal parameters are $C_1 \approx 0.073$ and $\alpha \approx 1.8$. (From Lovejoy and Schertzer, 2012a.) (b) Twenty-nine years years of NOAA's Climate Prediction Center (CPC) hourly US gridded precipitation data, (the number of data points used in the figure are $21 \times 13 \times 254040$ (east–west) $\times$ (north–south) $\times$ (time)). The intermittency near the mean is characterized by $C_1 = 0.37$ and the outerscale = 42 days. (Reproduced from Lovejoy and Schertzer, 2010.) (c)Spatial analysis of the trace moments of the flux estimated from the spatial Laplacian of the GEM u field at 850 mb at time step 00 h for $q = 0.0$ to 2.8 in increments of 0.2. (d) The 'universal' trace moments for quasi-Gaussian processes obtained from 100 realizations of an Ornstein–Uhlenbeck (OU) process with $\omega_0 = (128)^{-1}$ (grid points)$^{-1}$ using 100 realizations of process 2^{13} points long. This shows the moments up to order 2.9 at increments of 0.1 for an OU process, but the result is essentially identical to that of a pure Gaussian white noise (and to other quasi-Gaussian processes with $\beta < 4$). The lines correspond to $C_1 = 0.082$, $\alpha = 1.79$ and an outer scale of $\approx$ 10 pixels. The thick black lines compare the log–log linear fit for moments $q = 1.7$ for quasi-Gaussian processes (bottom) and Levy processes ($\alpha = 1.8$, top; moments for $q > \alpha$ are infinite). Even though the probability distribution is extreme, the outer scale increases to only 20 grid points and the non-dimensional $q = 1.7$ moment at the smallest scales is only about 50% larger. In order to obtain significantly stronger variability, strong long-range statistical dependencies are needed. (e) Schematic diagram of the space time-scales used here. To make the time axis dimensionally commensurate with the spatial axis, it has been multiplied by the mean transformation velocity estimated in section 5.2 (V_{trans}, is denoted as V in the figure). The raw model resolutions are the time step $V\tau_{\mathrm{st}}$ and the inner scale L_{i} (to simplify, we ignore the small difference between the inner analysis scale L_{i} and raw grid scale L_{st}: see Table 1). L_{ref} and τ_{ref} are the reference scales; $L_{\mathrm{ref}} = 20,000$ km and τ_{ref} varies from 223 days to 1000 days depending on the dataset. The vertical rectangles show the space–time averaging regions used to define the spatial flux averages using 'snapshots', whereas the horizontal rectangles show the space–time averaging regions used in the temporal analysis. The scales respect the inequalities $l \geq L_{\mathrm{i}} > V\tau_{\mathrm{st}}$ (spatial analyses) and $V\tau \geq V\tau_{\mathrm{i}} > L_{\mathrm{i}}$ (temporal analyses) as long as the $V_{\mathrm{i}} < V < V_{\mathrm{st}}$ (with $V_{\mathrm{i}} = L_{\mathrm{i}}/\tau_{\mathrm{i}}$, $V_{\mathrm{st}} = L_{\mathrm{i}}/\tau_{\mathrm{st}}$: see Table 1). This figure is available in colour online at wileyonlinelibrary.com/journal/qj

from September 1957 to August 2002 despite the changing observation network. The reanalyses were started every 6 h for every day: 0000 UTC, 0600 UTC, 1200 UTC and 1800 UTC. Reanalyses are clearly dependent not only on the data but also on the model being used for the assimilation, they are hybrid products.

This dataset was chosen because the data quality is relatively uniform over various multiyear periods. Reanalyses are important tools in meteorological and climatology research, and these data are easily compared with the other datasets analysed in this paper (in particular the analysis of each of the models). We analysed the most recent 3 yr of the reanalysis: September 1999 to August 2002 with a total of 4380 time steps analysed at 1000, 850, 700, 500 and 200 mb. See Uppala *et al.* (2005) for more details.

In the reanalysis the dynamic variables (i.e. wind/vorticity/divergence, temperature, humidity) are calculated on the T159 (triangular truncation up to wavenumber 159) spherical harmonic grid, while the other variables are on an N80 reduced Gaussian grid (80 latitudinal bands in each hemisphere with the number of points varying from 18 near the poles to 320 around the equator) on 60 vertical levels. The data were then interpolated onto a $1^\circ \times 1^\circ$ constant pressure level grid at the five pressure levels indicated above. Only the dynamic variables temperature (T), east–west (u) wind fields and specific humidity (h_s) are analysed. For the cascade analyses, data between 30°N– 30°S and 45°N–45°S were used. Although this interpolation causes the finest scales to be a little bit too smooth, problems such as aliasing are avoided.

3.2. *Discussion*

In attempting to determine the cascade structure we must consider the space–time resolution of the data – how large a region (in space and time) does each analysis element represent? Figure 3(e) shows the various scales on a schematic space–time diagram; in order to make the space and time axes commensurate, we have multiplied the times by a large-scale mean transformation velocity V_{trans} (estimated in section 5.2 below); this is adequate if the (horizontal) spatial and temporal exponents are equal (space–time is only 'trivially' anisotropic) so that the space–time relation is linear. This linearity is justified below on empirical grounds; in Lovejoy *et al.* (2008) it is given some theoretical justification (see also section 5). More generally, space–time can be scaling but anisotropic so that if the transformation is nonlinear (a power law), we need a generalized velocity; here we discuss the simplest linear case apparently relevant to the models.

Our analysis starts with the original raw model output that is at space–time resolution $L_{\text{i}}\times$ ($V_{\text{trans}}\tau_{\text{st}}$). We then estimate the turbulent fluxes either spatially by (absolute) finite difference Laplacian or temporally by (absolute) second-order time differences. In the spatial case, the flux is a dissipation-scale estimate and will have space–time resolution $L_{\text{i}}\times$ ($V_{\text{trans}}\tau_{\text{i}}$) with (see Table 1), $L_{\text{i}} > (V_{\text{trans}}\tau_{\text{i}})$, in the temporal case; because the available data are at either 6 or 12 h intervals ($\tau_{\text{i}} >> \tau_{\text{st}}$, see Table 1) and τ_{i} is in the scaling (not dissipation) range, we estimate temporal scaling fluxes (see section 2) at resolution $L_{\text{i}}\times$ ($V_{\text{trans}}\tau_{\text{i}}$) with ($V_{\text{trans}}\tau_{\text{i}}$) $> L_{\text{i}}$ (see Figure 3(e)). In both cases, the flux is estimated only by finite differences that involve neighbouring pixels, so that the fine-resolution fluxes may suffer from 'finite size effects', which become less and less important as their resolutions are degraded by subsequent spatial or temporal averaging. This presumably explains at least some of the deviations from scaling at the smallest space–time-scales. In addition, we have mentioned that the assumption that τ_{i} is in the scaling range is not perfect because the scaling will be perturbed by the assimilation cycle (6 h) as well as to varying degrees by the diurnal cycle. The latter effects can be minimized by first averaging four consecutive 6 h or two consecutive 12 h fields before the fluxes are estimated by differencing. However, this has the unfortunate effect of losing a factor of four (or two) in time-scales, which is quite a lot given that the temporal cascade begins to break down at scales of 1.5–10 days (τ_{dev}). In order to eliminate the effects of the diurnal cycle, we thus subtracted the mean of the dataset for the given time of the day.

Now consider the effect of degrading the resolution of the fine-scale flux estimates. The flux at a space–time resolution (l,τ) is a space–time flux average over the corresponding rectangles shown in the schematic. If $l >> V_{\text{trans}}\tau$, then the spatial resolution is dominant and the overall scale ratio is $\lambda = L_{\text{ref}}/l$. If on the contrary, $V_{\text{trans}}\tau >> l$, then the temporal averaging dominates and we obtain $\lambda = L_{\text{ref}}/(V_{\text{trans}}\tau)$; if the two are comparable, either can be used. From this, it is clear that the optimum is to choose the inner analysis resolutions to be comparable so that degrading purely in space or degrading purely in time gives us information about respectively the spatial and temporal structures. If – as suggested in the diagram – the temporal analysis resolution τ_{i} is too large, then at first ($l \approx L_{\text{i}}$) degrading in space will have little effect, it is only when $l >> V_{\text{trans}}\tau_{\text{i}}$ that the effect of spatial averaging will be felt.

A final comment about the temporal analysis is to signal the existence of a few missing fields for GEM. For the spatial scaling behaviour, this omission had only a negligible effect because each time step could be treated as a snapshot over which the spatial analysis technique could be applied independently. When determining the temporal behaviour, the analysis technique sees these holes. Because there were only a few missing time steps, it was decided that the missing data would be filled in by interpolation.

4. The temporal analyses

4.1. *Cascade analysis: forecast horizons, latitude and altitude dependence*

4.1.1. *t = 0*

Figures 4(a)–(f), 5(a)–(f), and 6(a)–(f) show the behaviour of the fluxes estimated using the absolute second-order difference at τ = 6 h (ERA40 and GFS) and 12 h (GEM). Each figure shows the horizontal wind, temperature and humidity moments (graphs top to bottom, (a)–(b), (c)–(d), (e)–(f), respectively) and at two pressure levels (1000 and 700 mb, left and right respectively) and for the statistical moments of order $q = 0.1, 0.2, \ldots, 2.9$ (for $q >\approx 0.5$, the slopes monotonically increase and for $0 < q < 1$ they are < 0, and for $q > 1$ they are > 0). We consider up to q = 2.9 only because the behaviour of larger moments is dominated by increasingly rare events and so the moments become less reliable. Note that the fields at 1000 mb are influenced by the generally higher quality data near the ground, although this is somewhat offset by the interpolation and extrapolation techniques needed when the topography is significant (i.e. 1000 mb often corresponds to points below ground). In addition, the diurnal cycle, which can lead to poor flux estimates (see above), is much stronger at 1000 mb (especially for the temperature). As stated earlier, we infer that there is a temporal cascade at smaller time-scales, of which we see only the longest time-scale in our analysis, because of the limited temporal resolution of the spatial cascade behaviour demonstrated in the spatial trace moments, as shown in Stolle *et al.* (2009). To compare with OU processes, the q = 2.9 moment of an OU process with $\omega_0 = \omega_{\text{max}}/64$ for each dataset is superimposed on the plots. As the flux is estimated by taking the absolute second difference – as discussed earlier this curve is quite insensitive to this transition scale – it is essentially universal for all quasi-Gaussian processes, at least those with small enough spectral slope (i.e. $\beta < 4$, because the second differencing is enough to flatten the spectrum of such processes).

The outer scale estimates for the various fields as functions of pressure level are given in Figure 7 we see that they are typically of the order of 10–20 days which is in fact of the order of the lifetime of an atmospheric structure (see the discussion below and Figure 7 for graphical results). We can also define a smaller scale at which the trace moments begin to deviate strongly from cascade behaviour. To quantify the deviations from Eq. (7) and to make this distinction more objective, we can define the deviations Δ from pure cascade behaviour using the formula:

$$\Delta = \overline{|\log_{10}(M_q) - K(q)\log_{10}(\lambda/\lambda_{\mathrm{eff}})|} \qquad (8)$$

where the overbar represents averaging over all the moments $q \leq 2$ and over the scale ratios $\lambda > \lambda_{\mathrm{dev}}$. If the range of scales used to estimate Δ is increased from the smallest scale (largest λ) to larger scales (smaller λ), we find that Δ starts off being relatively stable (i.e. the deviations are of roughly constant size) but at some point $\approx \tau_{\mathrm{dev}}$ it rapidly increases when the flux moments begin to deviate systematically from the scaling predictions of Eq. (8). Variable τ_{dev} can then be somewhat objectively defined as the scale at which Δ is 1.5 times the minimum value that it had in the smaller scale (cascade) region. Table 2 shows the variation of τ_{dev} for the various fields; we see that it is in the range $\approx$ 2–10 days, virtually independent of altitude (with the exception of the GEM T1000 mb field). Table 3 shows the cascade fit parameters for 1000 and 700 mb. Recalling that τ_{eff} is the effective outer cascade time-scale, in between τ_{eff} and τ_{dev}, the region is taken to be a transition region between weather and low frequency weather (Figures 4–6).

Before discussing the results further we note that in a few cases (especially the zonal wind) the variability is relatively small, so that it is worth considering the hypothesis that the data come from quasi-Gaussian processes, as discussed in section 2.3. A straightforward way to see this is to compare the trace moments (M) of the data with the 'universal' M for quasi-Gaussian processes (Figure 3(d)). Rather than crowd the figure with a direct superposition, we have indicated by dashed lines the expected outer scale (10 grid points) as well as the $q = 2.9$ maximum of $\log_{10}M$ ($= 0.46$). To further clarify this, the solid curved line shows the envelope of the OU moments up to $q = 2.9$. We can see that while the temperature and humidity fields are typically much more variable than a quasi-Gaussian process, especially at 1000 mb, the zonal wind is only somewhat more variable, therefore our conclusions are less strong with regard to the horizontal wind than for the other fields. The variability of the analysed fields becomes less at higher altitudes, meaning also that our conclusions are less strong at higher altitudes than at 1000 mb. It is not obvious how to come to more definite conclusions. For example, we may reproduce the OU process by using a stable Levy variable with infinite variance (i.e. $\alpha < 2$) in the place of the Gaussian. For those (finite) moments $q < \alpha$ it turns out that the trace moments are not very strongly affected – for example a Levy OU process with $\alpha = 1.8$ yields an outer scale of 20 pixels (rather than 10 for a Gaussian), and for $q = 1.7$ we have at a one grid point scale $\log_{10}M = 0.29$ rather than $\log_{10}M = 0.13$ for a Gaussian OU process. This indicates not only that strong variability at the smallest scales is important, but also that strong statistical independencies are necessary to produce large moments and outer scales significantly larger than 10–20 grid points.

Table 2. Estimate of τ_{dev} for GFS, GEM and ERA40 (roughly the same for all altitudes for each field); that is, scale at which $\Delta > 1.5$ times the minimum value.

τ_{dev} (days)	h	T	u
GFS	1.0–1.5	1.25	1.25
GEM	1.5–3.0	2.5–10.	1.5–3.0
ERA40	1.5–2.5	1.5	1.5

Considering the τ_{eff} estimates for the various fields, there are few obvious trends (see Figure 7). The main ones are: (i) the temperature tends to have a larger τ_{eff} than the other fields; (ii) ERA40 had generally smaller τ_{eff} than the other models; (iii) most of the estimates are on the order of 10 days, as expected based on the solar energy flux input and the horizontal scaling (see section 4.2); (iv) τ_{eff} for the lowest two altitudes of temperature for ERA40, temperature for the lowest altitude for GFS and the lowest altitude of temperature for GEM are much larger than the others.

4.2. *Differences in temporal cascade behaviour for 00 h and 48 h fields*

Figure 8(a)–(f) shows the effect of model integration when we compare analysis ($t = 0$) and 48 h forecast for the two forecast models. We see that there is very little difference between them. Apparently, the model integration has little effect on the cascades. Since the 48 h forecast is less affected by the initial data than the $t = 0$ fields, this gives some support to the idea that the long term 'climate' of the model also involves cascades possibly with very similar statistics. Before continuing we should mention that the regional dependence was also investigated by comparing the cascade structures for data between ±30° and ±45°. The differences in the cascade parameters were mostly small. In more systematic comparisons of this type (but on ECMWF interim reanalysis products) it was found that the main effect was on the outer time-scale, not the exponents, and that this variation followed fairly closely that predicted using the mean energy flux at the given latitude to predict the corresponding eddy turn-over time; see Lovejoy and Schertzer (2011) for more details.

4.3. *Levy collapse and universality*

We have been interested primarily in establishing the fundamental prediction of multiplicative cascade models Eq. (1a, 7). However, we also argued that there are basic physical, mathematical reasons (essentially the existence of a kind of multiplicative central limit theorem) that make it plausible that the model fields fall into special universality classes in which the basic scale invariant exponent $K(q)$ is given by Eq. (1b) characterized by just two parameters C_1 and α. In the analysis of spatial cascades (Stolle *et al.*, 2009) it was directly shown that universality works well – at least up to a critical moment q_c beyond which there is a 'multifractal phase transition' where $K(q)$ becomes asymptotically linear (a sample-size-dependent effect corresponding to the domination of the statistics

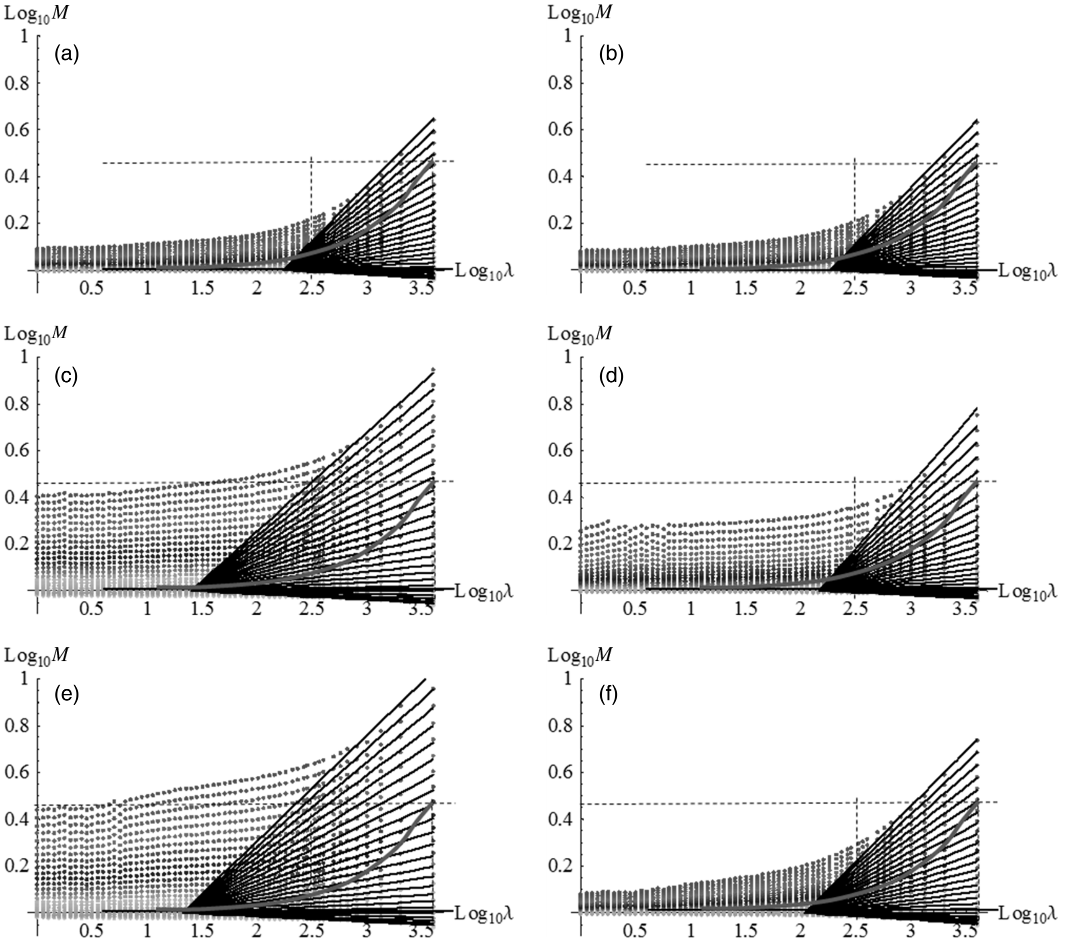

Figure 4. (a)–(f) Temporal fluxes estimated from the second-order differences (6 h resolution) in time, temporal trace moments ($q = 0.0$ to 2.9 in increments of 0.1) for ERA40 analysis between 30°N and 30°S. (a) u 1000 mb, $\tau_{\mathrm{eff}} = 5.8$ days, $\tau_{\mathrm{dev}} = 1.5$ days; (b) u 700 mb, $\tau_{\mathrm{eff}} = 5.4$ days, $\tau_{\mathrm{dev}} = 1.5$ days; (c) T 1000 mb, $\tau_{\mathrm{eff}} = 39.8$ days, $\tau_{\mathrm{dev}} = 1.5$ days; (d) T 700 mb, $\tau_{\mathrm{eff}} = 5.0$ days, $\tau_{\mathrm{dev}} = 1.5$ days; (e) h_s 1000 mb, $\tau_{\mathrm{eff}} = 47.9$ days, $\tau_{\mathrm{dev}} = 2.5$ days; (f) h_s 700 mb, $\tau_{\mathrm{eff}} = 9.2$ days, $\tau_{\mathrm{dev}} = 1.5$ days. $\tau_{\mathrm{ref}} = 1000$ days. Thick red reference curve is $q = 2.9$ moment of a Gaussian Ornstein–Uhlenbeck process (maximum of $\log_{10}M_{2.9} = 0.46$, $\tau_{\mathrm{eff}} = 2.5$ days). This figure is available in colour online at wileyonlinelibrary.com/journal/qj

Table 3. Estimates for α, C_1 and δ in GFS, GEM and ERA40 at 1000 and 700 mb (for use of δ see the caption of Figure 10). δ is the mean deviation over all time-scales.

Parameter	Dataset	h		T		u	
		1000	700	1000	700	1000	700
α	GFS	2.00	1.90	1.80	1.90	1.90	1.90
α	GEM	1.95	1.70	1.85	2.00	1.90	1.95
α	ERA40	2.00	1.75	1.90	1.90	1.90	1.90
C_1	GFS	0.108	0.124	0.114	0.110	0.136	0.109
C_1	GEM	0.091	0.097	0.080	0.101	0.121	0.116
C_1	ERA40	0.092	0.118	0.094	0.102	0.098	0.098
δ (%)	GFS	2.6	4.5	3.8	6.7	4.6	3.5
δ (%)	GEM	4.5	2.0	3.6	5.9	5.7	3.9
δ (%)	ERA40	3.6	2.2	3.5	5.6	4.7	3.4

by the largest flux values present (Schertzer *et al.*, 1993)). If the flux follows Eq. (1b) it implies that the generator of the cascade (log flux) is a Levy variable, index α. In that case, one can attempt to 'collapse' the moments M_q to a unique curve by dividing log M_q by the theoretical $K(q)$ for (say) $C_1 = 1$, i.e. by dividing it by $(q^\alpha - q)/(\alpha - 1)$; if M_q does indeed follow Eqs. (1a) and (1b) with parameters C_1 and α, then we obtain $\log M'_q = ((\alpha - 1)\ (\log M_q))/((q^\alpha - q)) = C_1 \log\lambda$, which is independent of the moment q so that all the curves with different q values 'collapse' onto a single curve with a slope that is given by C_1. The interest of such plots goes beyond just testing for the universal cascade behaviour: on a single plot we can independently evaluate both the scaling (the straightness of the collapsed lines) as well as the log-Levy nature of the generator – by the thinness of the collection of lines, i.e. how well at a given scale the different moments collapse, and how well they follow the form $(q^\alpha - q)$.

Before continuing we should mention that the stochastic cascade model that generates the 'weather' regime up to $\tau_{\mathrm{w}} \approx 10$ days (see Figure 1) can be extended to much longer time-scales, i.e. to scales where the space–time weather

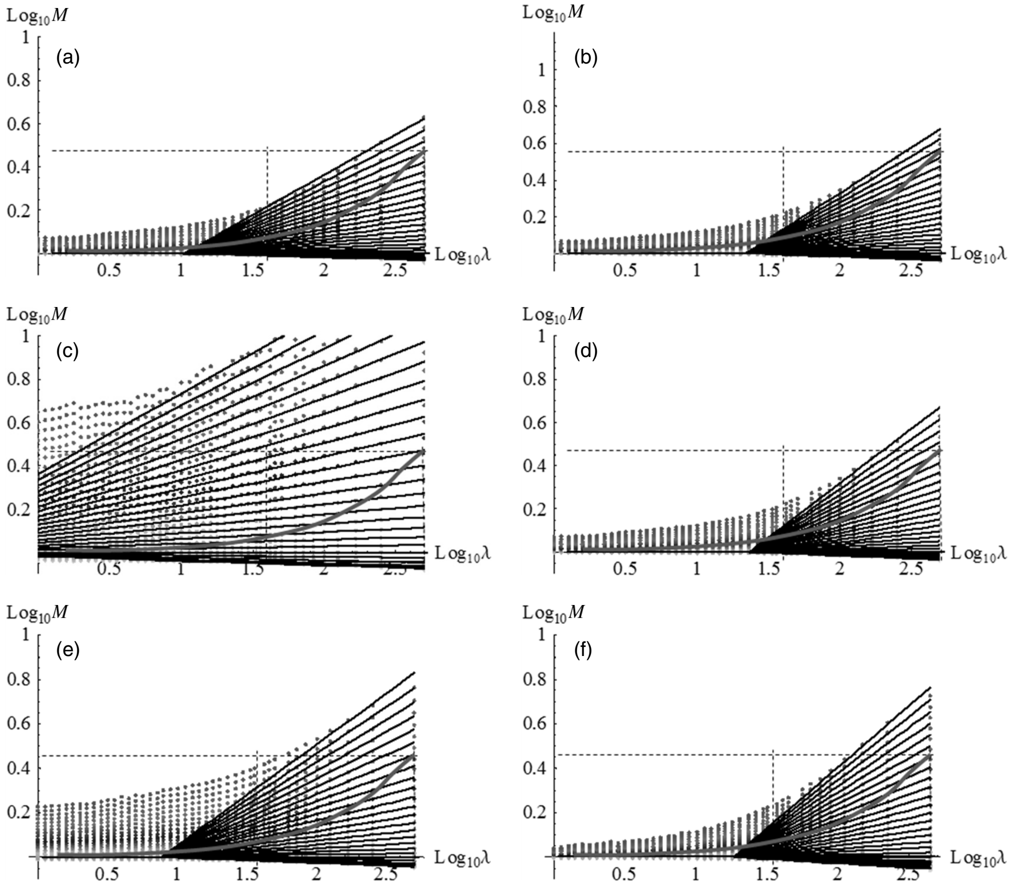

Figure 5. (a)–(f) Temporal flux estimated from absolute second-order differences in time (12 h resolution); trace moments ($q = 0.0$ to 2.9 in increments of 0.1) for GEM analysis between 30°N and 30°S. (a) u 1000 mb, $\tau_{\mathrm{eff}} = 24.2$ days, $\tau_{\mathrm{dev}} = 2.0$ days; (b) u 700 mb, $\tau_{\mathrm{eff}} = 10.2$, days, $\tau_{\mathrm{dev}} = 2.5$ days; c) T 1000 mb, $\tau_{\mathrm{eff}} = 2230$ days, $\tau_{\mathrm{dev}} = 10$ days; d) T 700 mb, $\tau_{\mathrm{eff}} = 9.6$ days, $\tau_{\mathrm{dev}} = 2.5$ days; (e) h_s 1000 mb, $\tau_{\mathrm{eff}} = 32.6$ days, $\tau_{\mathrm{dev}} = 1.5$ days; (f) h_s 700 mb, $\tau_{\mathrm{eff}} = 13.4$ days, $\tau_{\mathrm{dev}} = 3.0$ days. $\tau_{\mathrm{ref}} = 223$ days. Thick red reference curve is $q = 2.9$ moment of a Gaussian Ornstein–Uhlenbeck process (maximum of $\log_{10}M_{2.9} = 0.46$, $\tau_{\mathrm{eff}} = 5$ days). This figure is available in colour online at wileyonlinelibrary.com/journal/qj

cascade process has been reduced to an essentially purely temporal process. As argued in Lovejoy and Schertzer (2010), the collapse can be considered as a ‘dimensional transition’ where the model energy flux ε can be written as a product of high frequency space–time weather regime flux $\varepsilon_{\mathrm{w}}(\underline{r},t)$ multiplied by a low frequency weather process $\varepsilon_{\mathrm{lw}}(t)$ that is only a function of the time-scales longer than τ_{w}. Theory shows that $\varepsilon_{\mathrm{lw}}(t)$ has, at long enough scales, an asymptotically singular autocorrelation function $\langle\varepsilon_{\mathrm{lw}}(t)\varepsilon_{\mathrm{lw}}(t - \Delta t)\rangle \approx \Delta t^{-1}$; the corresponding spectrum has a low-frequency divergence. In practice this means that the spectrum $E(\omega)$ for frequencies lower than τ_{w}^{-1} will have spectral exponent β that depends only on the outer scale (and weakly on α), with realistic values in the range $\beta \approx 0.2$–0.4 (with $E(\omega) \approx \omega^{-\beta}$; this reproduces the observed low-frequency weather regime (see Lovejoy and Schertzer, 2012b; Figure 1).

Further consequences of the dimensional transition are that although the ‘bare’ low-frequency weather process $\varepsilon_{\mathrm{lw}}(t)$ process (i.e. constructed down to a given scale and stopped) has roughly log-Levy distributions, the empirically measured ‘dressed’ process (i.e. continued down to much smaller scales and then averaged as in our data analysis) will eventually have quasi-Gaussian statistics, therefore the Levy collapse would not continue to time-scales much longer than τ_{w}. However, as mentioned in the Introduction, this purely atmospheric model does not take into account interactions with the oceans, which apparently have similar turbulence and transitions, only with τ_{o} at about $\approx$ 1 yr (as mentioned in the Introduction $\varepsilon_{\mathrm{o}} \approx 10^{-8}\ \mathrm{m^2s^{-3}}$, which is much lower than $\varepsilon_{\mathrm{w}} \approx 10^{-3}\ \mathrm{m^2s^{-3}}$). The interaction between the ocean and the atmosphere may therefore provide the extra correlations needed to allow the log-Levy distributions to continue to longer time-scales of the order of one year.

With this theoretical motivation, let us turn to the analyses. In Figure 9 we see that the collapse for the different models and different fields is fairly convincing and this is out to scales well into the ‘climatological’ regime; typically the spread is 2–10% of the mean, comparable to that in space (see Stolle *et al.*, 2009), which we illustrate in Figure 10. Interestingly, temperature has the largest variability (highest curves) and humidity the lowest (except for the forecast models (GEM, GFS) at 1000 mb where the most variable field is the wind). Note that the largest deviations are at the very smallest scales (largest λ) due to the ‘finite size’ effects mentioned earlier, and at the very largest scales (smallest λ) where the statistics are poor.

Also indicated for reference are the curves indicating the envelope of the quasi-Gaussian processes (these all have $K(q) = 0$, see section 2.2 and Figure 3(c)), this essentially shows the rate of convergence of these non-intermittent non-cascade processes to the theoretical $K(q) = 0$ slope (with $\log M'_q = 0$). As seen in many of the cases (especially T and h), the empirical $\log M'_q$ curves are significantly above (i.e. they are more variable than) the quasi-Gaussian reference curves.

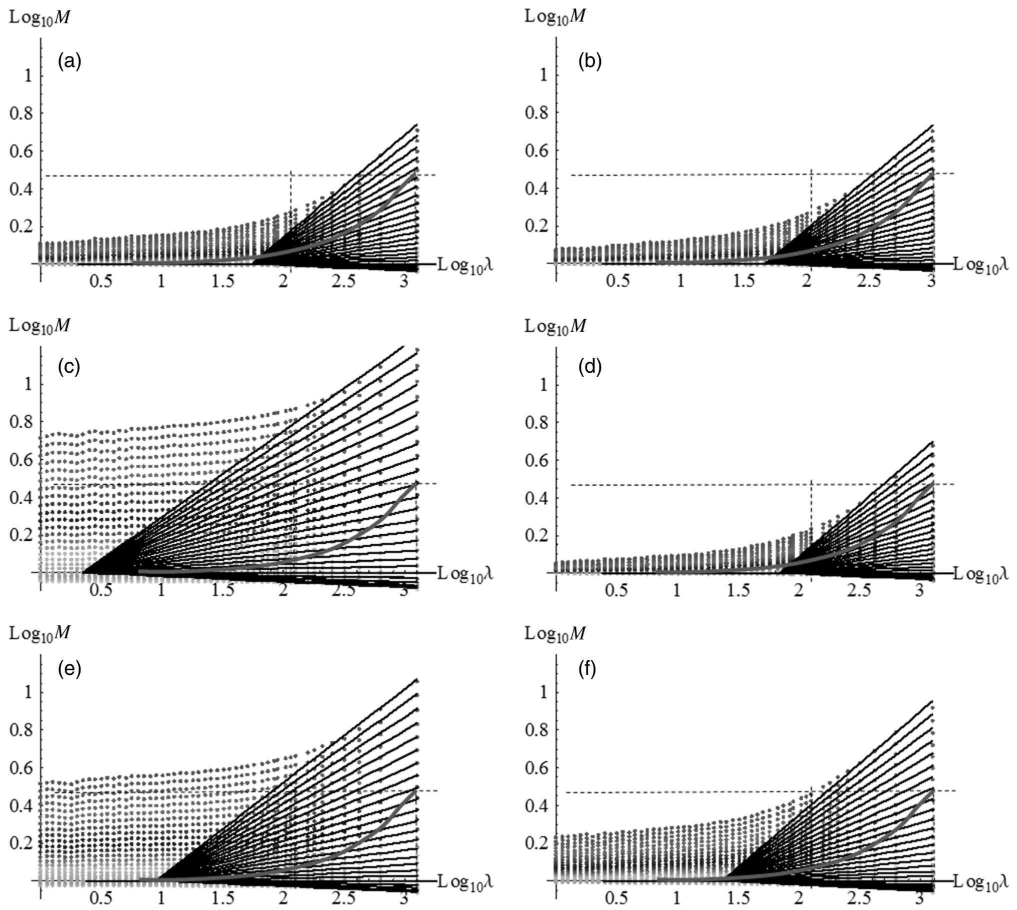

Figure 6. (a)–(f) Temporal flux estimated from the absolute second-order differences in time (6 h resolution); trace moments for GFS analysis between 30°N and 30°S. (a) u 1000 mb, $\tau_{\mathrm{eff}} = 5.8$ days, $\tau_{\mathrm{dev}} = 1.25$ days; (b) u 700 mb, $\tau_{\mathrm{eff}} = 23.4$ days, $\tau_{\mathrm{dev}} = 1.25$ days; (c) T 1000 mb, $\tau_{\mathrm{eff}} = 141.2$ days, $\tau_{\mathrm{dev}} = 1.25$ days; (d) T 700 mb, $\tau_{\mathrm{eff}} = 4.5$ days, $\tau_{\mathrm{eff}} = 1.25$ days; (e) h_r 1000 mb, $\tau_{\mathrm{eff}} = 35.5$ days, $\tau_{\mathrm{dev}} = 1.25$ days; (f) h_r 700 mb, $\tau_{\mathrm{eff}} = 13.5$ days, $\tau_{\mathrm{dev}} = 1.25$ days. $\tau_{\mathrm{ref}} = 300$ days. Thick red reference curve is $q = 2.9$ moment of a Gaussian Ornstein–Uhlenbeck process (maximum of $\log_{10} M_{2.9} = 0.46$, $\tau_{\mathrm{eff}} = 2.5$ days). This figure is available in colour online at wileyonlinelibrary.com/journal/qj

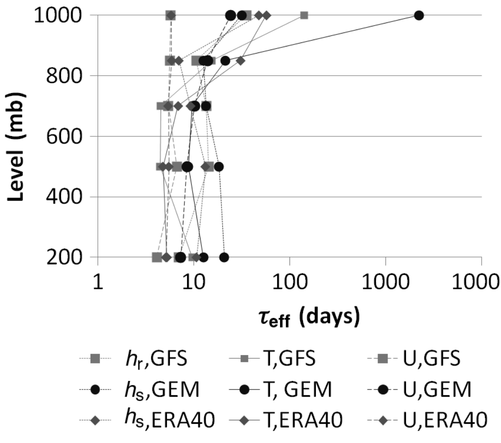

Figure 7. Estimates of τ_{eff} for GFS (green lines, square points), GEM (blue lines, circular points), ERA40 (red lines, diamond points) for t = 00 h. The lines indicate which points belong to the same dataset/field h (short dashed lines), T (solid lines), u (long dashed lines). This figure is available in colour online at wileyonlinelibrary.com/journal/qj

5. Comparing the spatial and temporal cascades

5.1. *Spatial analyses using spatial and temporal flux estimates*

We noted in section 2 that turbulent fluxes could be estimated by using either (horizontal) spatial Laplacians (as in the analysis of Stolle *et al.* (2009)) or by second-order differences in time (the discrete Laplacian analogue). However, the fluxes estimated in space and in time are not necessarily the same, notably because the spatial estimates are at the (model) dissipation scale whereas the temporal estimates are in the scaling regime (with the caveats about the diurnal and assimilation cycles mentioned earlier). In section 2 we argued that if the normalized spatial and temporal fluxes are different powers of the underlying flux (say $\varphi_x = \varepsilon^{\eta_x} / <\varepsilon^{\eta_x}>, \varphi_t = \varepsilon^{\eta_t} / <\varepsilon^{\eta_t}>$ in space and time respectively), then if ε are also universal multifractals with index α, then the ratio $\log <\varphi_x^q> / \log <\varphi_t^q> = (\eta_x/\eta_t)^{\alpha}$; i.e. they are in a constant ratio. In Figure 11 we rescaled the φ_t moments by taking the optimum powers of the moments of the temporal fluxes so that they optimally overlap the φ_x moments. We see that there is generally good agreement between the rescaled temporal fluxes and the spatial fluxes. The fluxes estimated in the time domain assume that the latter is in a scaling regime at the 6 h (or 12 h for GEM) time-scale used for estimating the second-order differences. However, the flux estimate may be poor due to the non-scaling perturbations, such as the assimilation or the diurnal cycle. The fact that generally the degree of overlap is very high gives us confidence that the flux estimates are robust. Indeed, we see that the main case of poor overlap is precisely the 1000 mb T fluxes, which are particularly affected by the diurnal cycle. In Table 4 we see that the ratio is close to unity (with the exception of u at 1000 mb and GFS h_r), with GEM

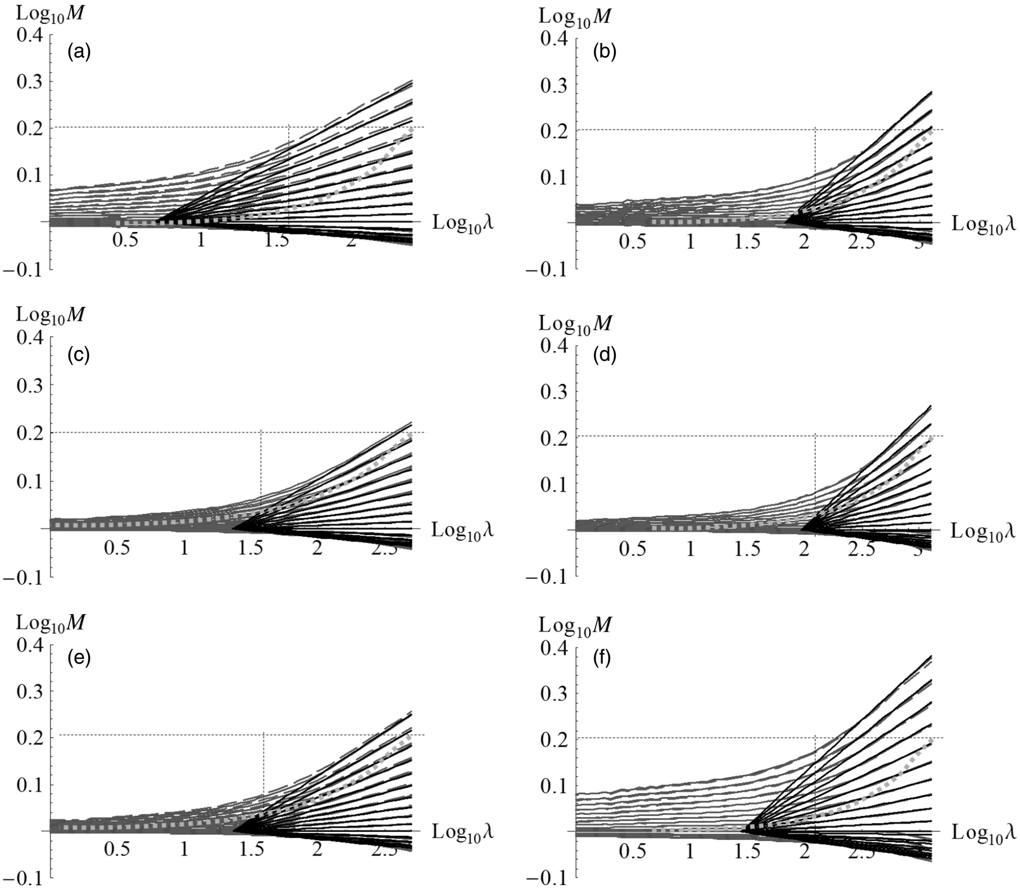

Figure 8. (a)–(f) Temporal flux, temporal trace moments (q = 0.0 to 2.0 in steps of 0.1) for GEM (T_{ref} = 223 days, 12 h resolution) and GFS (T_{ref} = 223 days, 6 h resolution) between 30°N and 30°S at $t = 0$ (solid red) and t = 48 h (dashed blue). (a) GEM u 1000 mb; (b) GFS u 1000 mb; (c) GEM T 700 mb; (d) GFS T 700 mb; (e) GEM h_s 700; (f) GFS h_r 700 mb. Dotted green reference curve is q = 2.0 moment of a Gaussian Ornstein–Uhlenbeck process (maximum of $\log_{10}M_{2.0} = 0.20$, τ_{eff} = 2.5 days (for GFS) and 5.0 days (for GEM)). This figure is available in colour online at wileyonlinelibrary.com/journal/qj

Table 4. Ratio, $\log< \varphi_x^q > /log < \varphi_t^q >$connecting the space and time fluxes according to theory, this equals $(\eta_x/\eta_t)^{\alpha}$.

Dataset	$\log < \varphi_x^q > /\log < \varphi_t^q >$		
	u	T	h
ERA40 1000 mb	1.6	1.1	1.0
ERA40 700 mb	1.4	1.4	1.0
GEM 1000 mb	0.7	1.1	0.8
GEM 700 mb	0.7	1.0	0.8
GFS 1000 mb	1.6	1.6	2.0
GFS 7000 mb	1.0	1.0	1.0

having slightly smaller values (∼0.7), GFS averaging to a little above 1 between the different fields (although the ratio for the 1000 mb h_r field is about 2), and the average of the values for ERA40 being slightly larger than 1. As $\alpha \approx 1.8$ for all the fields, for GEM this corresponds to $\eta_x/\eta_t \approx 0.85$. This is close enough to the value 1 that it is possible that all the results are compatible with 1, with the small differences due to some other cause. Recall that $\eta_x = \eta_t = 1/2$ (hence $\eta_x/\eta_t = 1$) in the case of the energy flux estimated at the dissipation scale in space and in the Lagrangian scaling regime in time. Note that we use the 6 h fluxes as opposed to the 1 day fluxes for GFS and ERA40 because it allows for a larger range of analysis; this procedure is validated in Figure 11.

5.2. *Space–time diagrams*

In order to systematically explore the space–time relations we can compare the statistics of the flux moments as functions of time-scale and as functions of space-scale; it is important that we degrade the same flux in both space and in time. The previous subsection showed that both the spatial finite difference Laplacian or the second-order temporal difference give essentially equivalent results (related by a factor close to unity to go from one to the other due to the different fluxes that are estimated). We therefore chose to use the absolute second-order temporal differences and estimate the space–time ('Stommel') diagrams for the various fields using the following method. The basic idea is that if for a spatial scale L and a temporal scale τ and for all q, we have

$$\langle \varepsilon^q_{\tau_{\mathrm{ref}}/\tau} \rangle = \langle \varepsilon^q_{L_{\mathrm{ref}}/L} \rangle. \tag{9}$$

then the scales L and τ are implicitly equivalent in the sense that their statistics are the same; for example, if Eq. (9) holds for all q then at the level of random variables it implies: $\varepsilon_{\tau_{\mathrm{ref}}/\tau} \overset{d}{=} \varepsilon_{L_{\mathrm{ref}}/L}$, where '$\overset{d}{=}$' means equality of probability distributions.

If the horizontal scaling of the flux is the same as the temporal scaling the same flux, then to determine the relation between τ and L it suffices to superpose the spatial and temporal M_q and adjust them left–right on the log–log

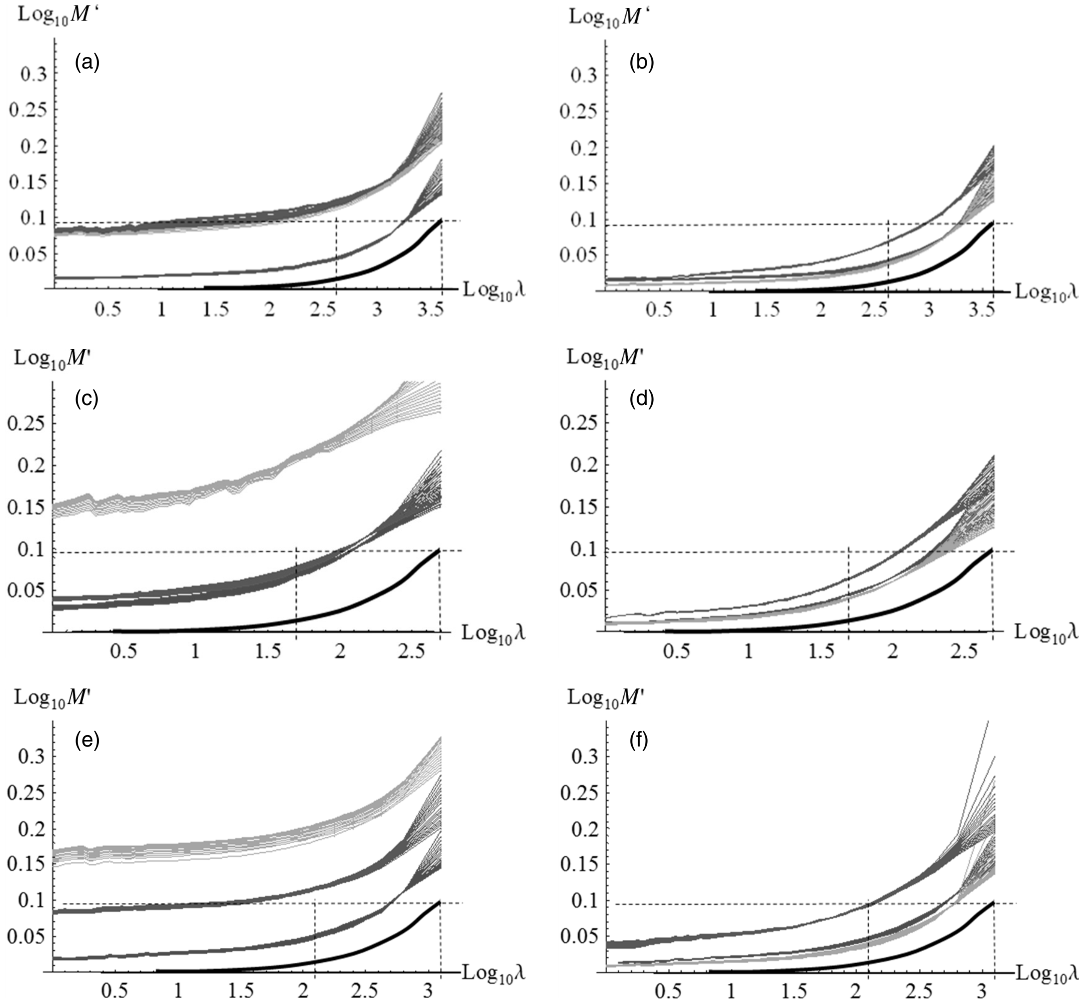

Figure 9. (a)–(f) Levy collapse ($Log_{10}M'_q = (\alpha - 1)(Log_{10}M_q)/(q^\alpha - q)$) of temporal flux, of the temporal trace moments at $t = 0$ h ($q = 0.1$ to 2.0 excluding $q = 1.0$) for ERA40 ($\tau_{\mathrm{ref}} = 1$ yr), GEM ($\tau_{\mathrm{ref}} = 223$ days), and GFS ($\tau_{\mathrm{ref}} = 300$ days, except u 700 mb, $\tau_{\mathrm{ref}} = 250$ days) analysis between 30°N and 30°S of u (red, darkest shade), T (green, lightest shade), h_r or h_s (blue, middle shade). (a) ERA40 1000 mb, (b) ERA40 700 mb, (c) GEM 1000 mb, (d) GEM 700, (e) GFS 1000 mb and (f) GFS 700 mb. The collapse is visible by the bunching, overlap of the curves. For comparison we have also indicated the envelope in black of logM' for quasi-Gaussian processes (collapsed using $\alpha = 1.8$), indicating their convergence to the theoretical log$M' = 0$ asymptote for small λ. The values of α used are given in Table 3. This figure is available in colour online at wileyonlinelibrary.com/journal/qj

plot to find the optimum space–time ratio (i.e. velocity) connecting them. If the scaling between space and time is anisotropic, i.e. $(\tau_{\mathrm{ref}}/\tau) = (L_{\mathrm{ref}}/L)^{H_t}$ with $H_t \neq 1$, then the space–time relation is nonlinear; see Radkevitch *et al.* (2008) for a discussion and space–time analysis of lidar backscatter data). Theoretically, there are two classic possibilities for H_t: if we ignore advection, then for the horizontal wind field dominated by the turbulent energy flux, ε, in space the (Kolmogorov) scaling is $\Delta v \approx \varepsilon^{1/3}\Delta x^{1/3}$, whereas the corresponding (Lagrangian frame) formula in time is $\Delta v \approx \varepsilon^{1/2}\Delta t^{1/2}$. This leads to $H_t = (1/2)/(1/3) = 2/3$. However, even if there is no imposed large-scale wind, the (random) largest planetary scale eddies will advect all the smaller scale eddies, and this would be up to the outer scale of the scaling regime (here, planetary in extent). This advection will lead to $H_t = 1$, with the overall advection velocity being the large-scale turbulent velocity mentioned earlier: $V \approx \varepsilon^{1/3}L_{\mathrm{eff}}^{1/3}$. This argument is an extension of one first invoked by Tennekes (1975); see the discussion in Lovejoy *et al.* (2008). Figure 12(a) shows a typical result when the technique is applied to the hourly resolution infraradiances (see Figure 1). We see that the space–time relation is roughly linear up to 2 days in the north–south direction and nearly 10 days in the east–west direction.

Once again, the difficulty with calculating space–time diagrams for the model outputs is that the temporal resolution is barely adequate. Figures 13(a)–(f) show the results for 1000 mb and 700 mb for all of the datasets. In addition, the single smallest scale point, corresponding to 6 h (or 12 h for GEM) in time (for which the fluxes are not necessarily well estimated due to 'finite size effects'), is also a little too low. The space–time relation is not as linear as in Figure 12(a) or as was found in the ECMWF interim reanalyses in Lovejoy and Schertzer (2011), reproduced for comparison in Figure 12(b). We seem to have deviations at small Δt due to finite size effects, a narrow scaling regime ($\approx$ 12 h to 2 days), and then the beginning of the low-frequency weather regime. The reference lines in Figure 13 are plausible given 'finite size effects' affecting the smallest time steps (6 and 12 h) and the small range of the temporal scaling.

A transition to the low-frequency weather regime is easily seen on the space–time diagrams by the flattening of the curves. Overall GEM shows a clearer transition at 1000 mb than at 700 mb despite the noisier space–time diagram. In addition, the corresponding advection velocities are around

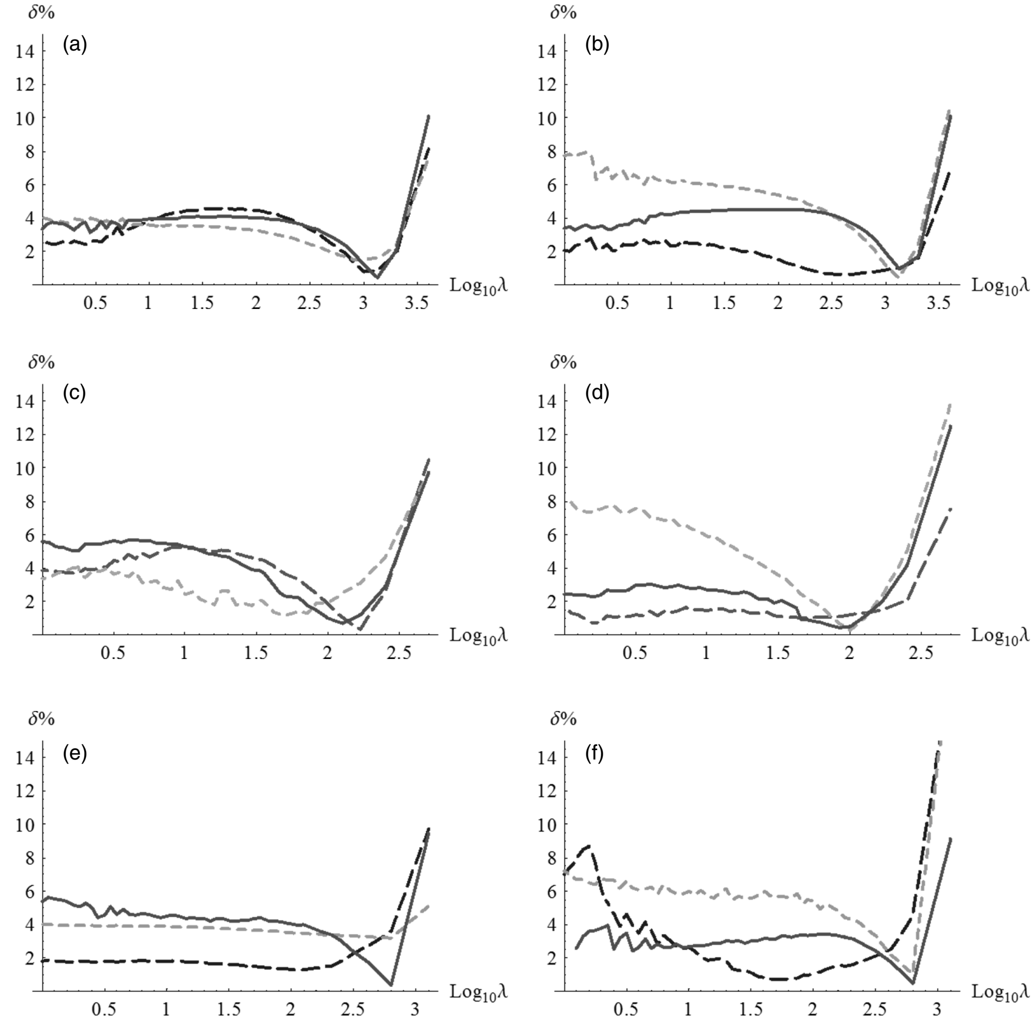

Figure 10. (a)–(f) The relative root mean square spread of the Levy collapse of Figure 9 (δ, the relative standard deviation of $log_{10}M'_q = (\alpha-1)(log_{10}M_q)/(q^\alpha - q)$ of temporal flux for $q = 0.1$ to 2.0 excluding $q = 1.0$) for ERA40 ($\tau_{\mathrm{ref}} = 1$ yr), GEM ($T_{\mathrm{ref}} = 223$ days) and GFS ($\tau_{\mathrm{ref}} = 300$ days, except u700 mb, $\tau_{\mathrm{ref}} = 250$ days) analysis between 30°N and 30°S of u (red, solid), T (green, short dashes), h_r or h_s (blue, long dashes). (a) ERA40 1000 mb, (b) ERA40 700 mb, (c) GEM 1000 mb, (d) GEM 700, (e) GFS 1000 mb and (f) GFS 700 mb. The collapse corresponds to small values of δ. The mean δ is given in Table 3. This figure is available in colour online at wileyonlinelibrary.com/journal/qj

500–1000 km day^{-1} for GFS and ERA40, which are close to that found in the analysis of geostationary infrared satellite imagery (Figure 12(a)) and close to those estimated from the solar energy injection as discussed in section 4.2. The GEM, on the other hand, has a characteristic velocity of 250 km day^{-1} at 1000 mb, which is somewhat smaller though perhaps not inconsistent. With the exception of the GFS 1000 mb and GEM 1000 mb fields, the wind, humidity and temperature have very similar space–time transformation velocities (V_{trans}).

As seen in the space–time diagrams (ignoring the exceptions in GFS 1000 mb and GEM 700 mb), they start to level off at around 5000–10000 km corresponding to ≈ 10 days. This is about the size of the accurate temporal scaling regime, τ_{dev} (1.5–6.0 days) – the scaling value where the trace moments were found to deviate from cascade behaviour. The difference between τ_{dev} and the value at which the space–time diagrams flatten differ because both the spatial and temporal trace moments tend to curve at the largest scales, so that the space–time diagrams could nevertheless have a linear part over a wider range than the scaling in either space or in time. When the space–time curves become flat, the low-frequency weather regime begins.

6. Conclusions

Cascades and brute force numerical approaches to modelling and understanding the atmosphere have coexisted ever since Richardson in the 1920s. Today, the divorce between these approaches is such that atmospheric scientists use only rather vague cascade ideas based largely on dimensional analysis coupled with strong assumptions about isotropy (in either two or three dimensions), while turbulence scientists focus on verifying the predictions of multiplicative cascades in laboratory experiments, usually – unfortunately – with similarly strong isotropy assumptions. However, due to gravity, Coriolis and other forces and boundary conditions, the atmosphere is anisotropic, yet it is nevertheless scaling over wide ranges of scale. This conclusion has been supported by satellite imagery, meteorological reanalyses and *in situ* aircraft studies. In particular, the scaling of the vertical stratification allows the atmosphere to have cascades acting over huge ranges of scale.

In a recent paper (Stolle *et al.*, 2009) we studied the spatial cascade structure of the temperature, humidity and horizontal wind for ERA40 reanalyses and for GFS and GEM forecast models, and found that up to scales of about 5000 km for various altitudes, latitudes and forecast times,

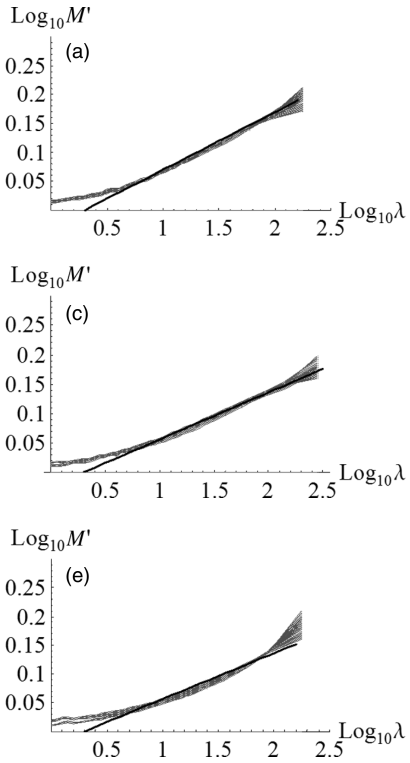

Figure 11. (a)–(f) The mean Levy collapse $log_{10}M_q' = (\alpha - 1)(log_{10}M_q)/(q^\alpha - q)$ of spatial scaling of the fluxes estimated from the spatial Laplacian flux (red, darker shade) and temporal second-order difference flux (blue, lighter shade) spatial trace moments at $t = 0$ h ($q = 0.1$ to 2.0 excluding $q = 1.0$) for ERA40 ($T_{\mathrm{ref}} = 1$ yr), GEM ($T_{\mathrm{ref}} = 223$ days) and GFS ($T_{\mathrm{ref}} = 300$ days, except u 700 mb, $T_{\mathrm{ref}} = 250$ days) analysis between 30°N and 30°S. The time trace moment is multiplied by the factor $(\eta_x/\eta_t)^\alpha$ given in Table 4. (a) ERA40 u 1000 mb; (b) ERA40 T 700 mb; (c) GEM u 1000 mb; (d) GEM h_s 700; (e) GFS u 1000 mb; (f) GFS h 700 m. The slopes are $C_1 = K(q)/(q^\alpha - q)$ of the spatial trace moments are the same as in Stolle *et al.* (2009), with α taken from there. This figure is available in colour online at wileyonlinelibrary.com/journal/qj

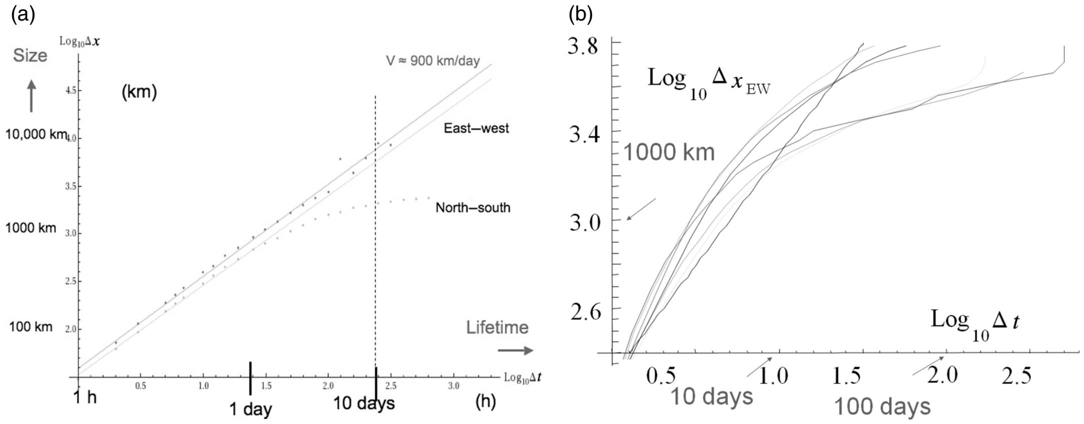

Figure 12. (a) The horizontal space–time diagram constructed by comparing the temporal MTSAT cascades (Figure 1) and north–south and east–west analyses of the corresponding spatial moments. Over the scales where the data are linear, spatial and temporal statistics (for the q = 2 moment) are related by a constant velocity of ≈ 900 km day^{-1}. (From Lovejoy and Schertzer, 2010.) (b) Space–time plots for the ECMWF interim reanalysis for 700 mb fields analysed for 2006 using the $q = 2$ moments and using $\lambda = T_{\mathrm{ref}}/\Delta t$ and $\lambda = L_{\mathrm{ref}}/\Delta x$ for time and space respectively (east–west and time). Yellow = h_s, green = T, cyan = u, blue = v, purple = w, red = z. The black reference line has a slope 1; it corresponds to a speed of ≈ 225 km day^{-1}; the spread in the lines indicates a variation over a factor of about 1.6 in speed. (Reproduced from Lovejoy and Schertzer, 2012b). This figure is available in colour online at wileyonlinelibrary.com/journal/qj

the predictions of multiplicative cascade models are satisfied to typically ±1% (for moments up to second order). In this article we extend these analyses to the time domain. A key difficulty of these analyses, when compared with either the corresponding spatial analyses or with many of the empirical analyses, is that the ratio of the outer scale of the weather variability (τ_{w} corresponding, as we argue, to the lifetime/'eddy turn-over time' of planetary scale eddies) to the model resolutions (τ_{i}) is quite small (e.g. ≈ (5 days)/(12 h) ≈ 10 or less) so that the scaling itself is not so convincing, but also the accuracy of the exponent estimates is not high. For example, although the temporal cascades typically have effective outer scales τ_{eff} of around 15 days, the scaling starts to worsen for scales greater than τ_{dev} of ≈ 1.25–10 days. Indeed, to make the existence of the temporal cascades more convincing we showed two examples of temporal cascades from hourly resolution data (infrared imagery and rain rates), and also systematically compared our model moment analyses with those from quasi-Gaussian processes (which included

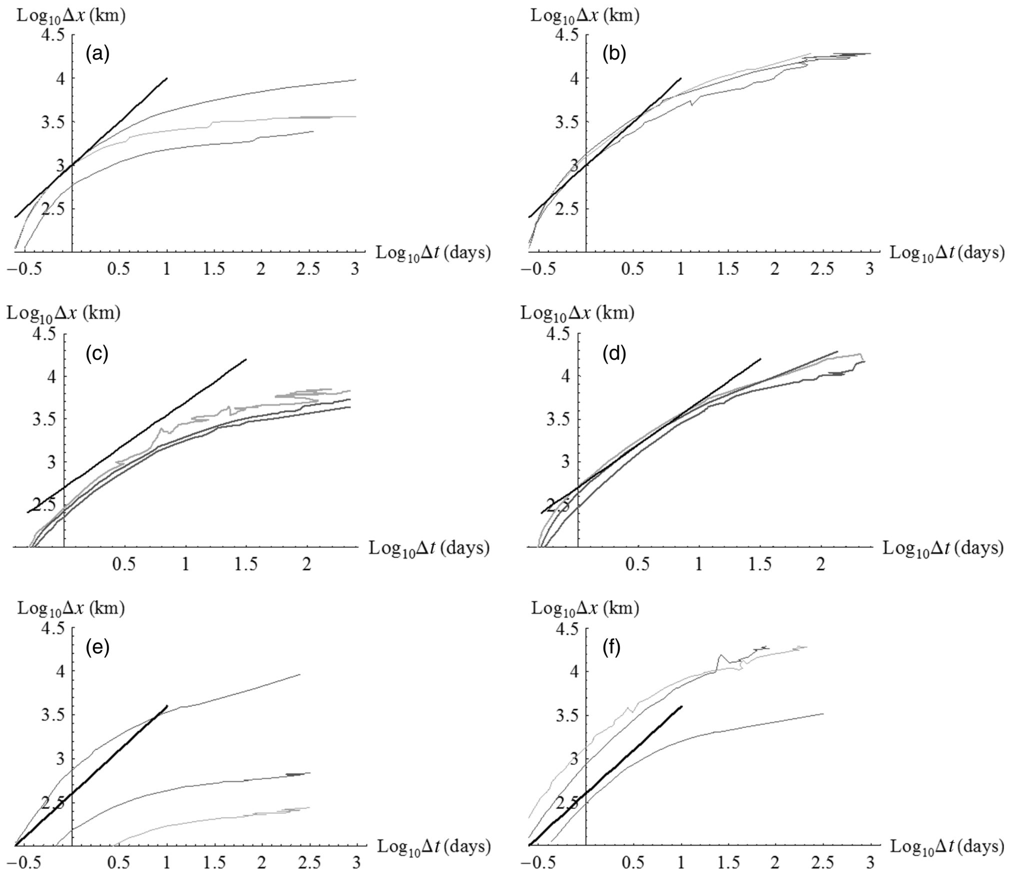

Figure 13. (a)–(f) Space–time (Stommel) diagrams based on $q = 2.0$ moments using absolute second temporal difference flux estimate at $t = 0$ h ($q = 0.1$ to 2.0 excluding $q = 1.0$) for ERA40 and GFS analysis between 30°N and 30°S of u (red, darkest shade), T (green, lightest shade), h_r or h_s (blue, intermediate shade). The black line with slope $H_t = 1$ represents the magnitude of the 'typical' transformation velocity. (a) ERA40 1000 mb, $V_{\mathrm{trans}} = 1000$ km day^{-1}; (b) ERA40 700 mb, $V_{\mathrm{trans}} = 1000$ km day^{-1}; (c) GEM 1000 mb, $V_{\mathrm{trans}} = 500$ km day^{-1}; (d) GEM 700 mb, $V_{\mathrm{trans}} = 500$ km day^{-1}; (e) GFS 1000 mb, $V_{\mathrm{trans}} = 450$ km day^{-1}; (f) GFS 700 mb, $V_{\mathrm{trans}} = 450$ km day^{-1}. This figure is available in colour online at wileyonlinelibrary.com/journal/qj

Ornstein-Uhlenbeck processes that are essentially integrals of Gaussian white noises and which are sometimes used as models). The non-dimensional statistical moments of quasi-Gaussian processes take roughly a factor of 10 in time-scale to converge so that they are not necessarily easy to distinguish from cascade processes analysed over small ranges of scale. Nevertheless, especially for the temperature and humidity fields, the variability of the model outputs was significantly higher than for quasi-Gaussian processes, the latter being unable to reproduce the observed variability. These conclusions were supported by the analysis of 'Levy collapses' of the temporal moments, which indicate that the generators (logs) of the fluxes are of the predicted 'universal' Levy form even outside the scaling regime.

By comparing the spatial and temporal cascade structures we can deduce statistical relations between space and time, and therefore construct space–time diagrams. If there is scaling in space and in time, then the resulting space–time diagrams will be scaling. Unfortunately, because the temporal scaling regime is narrow the scaling of the space–time relations is poor (the corresponding ECMWF interim relations are much more convincing in this regard), although we obtain space–time transformation velocities in the realistic range 250–1000 km days^{-1}.

The close equivalence between deterministic models and stochastic cascades opens up new avenues in atmospheric science; this is particularly true since the goal of weather modelling today is increasingly a stochastic one with ensemble forecasting systems becoming the norm. At the moment there is a growing need to obtain stochastic descriptions of these deterministic systems, for example, in choosing the ensemble initializations as in the *ad hoc* methods of Corazza *et al.* (2003)) as well as in 'stochastic parametrization' of the subgrid effects, which are currently fairly *ad hoc* (Buizza *et al.*, 1999; Palmer, 2001). Direct exploitation of the known cascade structures presumably would be of great immediate benefit. However, looking further into the future, rather than making cumbersome attempts to add randomness to a fundamentally deterministic system, it may be preferable to use the cascades as a basis of direct stochastic forecasting in which information on the state of the weather at $t = 0$ is used to directly estimate the conditional probabilities (or conditional expectations) of the weather over various forecast horizons. Cascade-based pure stochastic approaches would have the advantage of being able to (statistically) account for huge ranges of scales as well as to be able to make forecasts at any desired resolution.

Acknowledgements

We would like to acknowledge NSERC for Jonathan Stolle's scholarship support as well as Dr Michel Bourqui, Dr Andrew Ryzkhov and Dr Charles Lin for their helpful discussions and technical expertise. The analysis of GEM data was based on Environment Canada data and the ERA40 data developed by the ECMWF, and the GFS data were obtained through UCAR. We thank J. Pinel for Figure 12(a). This research did not enjoy any specific funding.

References

Anselmet F, Antonia RA, Danaila L. 2001. Turbulent flows and intermittency in laboratory experiments. *Plan. Space Sci.* **49**: 1177–1191, DOI: http://dx.doi.org/10.1016/S0032-0633(01)00059-9.

Buizza R, Miller M, Palmer TN. 1999. Stochastic representation of model uncertainties in the ECMWF ensemble prediction system. *Q. J. R. Meteorol. Soc.* **125**: 2887–2908, DOI: 10.1002/qj.49712556006.

Bunde A, Eichner JF, Havlin S, Koscielny-Bunde E, Schellnhuber HJ, and Vyushin D. 2004. Comment on 'Scaling of Atmosphere and Ocean Temperature Correlations in 1145 observations and Climate Models'. *Phys. Rev. Lett.* **92**: 039801, DOI: 10.1103/PhysRevLett.92.039801.

CMC. 2009a. *High-resolution GRIB Dataset*. http://www.weatheroffice.gc.ca/grib/High-resolution_GRIB_e.html (accessed 6 February 2009)

CMC. 2009b. *Global Data Assimilation System (DAS)*. http://www.meted.ucar.edu/nwp/pcu2/GEMglobal/gemglobassim.htm (accessed 22 July 2009)

Corazza M, Kalnay E, Patil DJ, Morss R, Szunyogh I, Hunt BR, Ott E, Cai M. 2003. Use of the breeding technique to estimate the structure of the analysis 'errors of the day'. *Nonlin. Proc. Geophys.* **10**: 233–243, DOI: 10.5194/npg-10-233-2003.

Côté J, Desmarais JD, Gravel S, Méthot A, Patoine A, Roch M, Staniforth A. 1998a. The operational CMC-MRB global environmental multiscale (GEM) model. Part II: Results. *Mon Weather Rev*. **126**: 1397–1418, DOI: 10.1175/1520-0493(1998)126<1397:TOCMGE>2.0.CO;2.

Côté J, Gravel S, Méthot A, Patoine A, Roch M, Staniforth A. 1998b. The operational CMC-MRB global environmental multiscale (GEM) model. Part I: Design considerations and formulation. *Mon. Weather Rev.* **126**: 1373–1395, DOI: 10.1175/1520-0493(1998)126<1373:TOCMGE>2.0.CO;2.

Eichner JF, Koscielny-Bunde E, Bunde A, Havlin S, Schellnhuber HJ. 2003. Power-law persistence and trends in the atmosphere: A detailed study of long temperature records. *Phys. Rev. E.* **68**: 046133, DOI: 10.1103/PhysRevE.68.046133.

Fraedrich K, Blender R. 2003. Scaling of Atmosphere and Ocean Temperature Correlations in Observations and Climate Models. *Phys. Rev. Lett.* **90**: 108501, DOI: 10.1103/PhysRevLett.90.108501.

Huybers P, Curry W. 2006. Links between annual, Milankovitch and continuum temperature variability. *Nature* **441**: 329–332, DOI: 10.1038/nature04745.

Inoue E. 1951. On the turbulent diffusion in the atmosphere. *J. Meteorol. Soc. Jpn* **29**: 59–66.

Koscielny-Bunde E, Bunde A, Havlin S, Roman HE, Goldreich Y, Schellnhuber H-J. 1998. Indication of a universal persistence law governing atmospheric variability. *Phys. Rev. Lett.* **81**: 729–732, DOI: 10.1103/PhysRevLett.81.729.

Landau LD, Lifschitz EM. 1959. *Fluid Mechanics*. Pergamon: London; 116–128.

Lovejoy S, Schertzer D. 1986. Scale invariance in climatological temperatures and the spectral plateau. *Ann Geophys* **4B**: 401–410.

Lovejoy S, Schertzer D. 2010. Towards a new synthesis for atmospheric dynamics: space–time cascades. *Atmos. Res.* **96**: 1–52, DOI: 10.1016/j.atmosres.2010.1001.1004.

Lovejoy S, Schertzer D. 2011. Space–time cascades and the scaling of ECMWF reanalyses: fluxes and fields. *J. Geophys. Res.* **116**: D14117, DOI: 10.1029/2011JD015654.

Lovejoy S, Schertzer D. 2012a. *The Weather and Climate: Emergent Laws and Multifractal Cascades*. Cambridge University Press: Cambridge; 660 pp.

Lovejoy S, Schertzer D. 2012b. Low frequency weather and the emergence of the climate. In *Complexity and Extreme Events in Geosciences*, Sharma AS, Bunde A, Baker D, Dimri VP (eds). AGU Monographs (in press).

Lovejoy S, Tuck AF, Hovde SJ, Schertzer D. 2007. Is isotropic turbulence relevant in the atmosphere? *Geophys. Res. Lett.* **34**: L14802, DOI: 10.1029/2007GL029359.

Lovejoy S, Schertzer D, Lilley M, Strawbridge KB, Radkevitch A. 2008. Scaling turbulent atmospheric stratification, Part I: turbulence and waves. *Q. J. R. Meteorol. Soc.* **134**: 277–300, DOI: 10.1002/qj.201.

Lovejoy S, Tuck AF, Hovde SJ, Schertzer D. 2009a. The vertical cascade structure of the atmosphere and multifractal drop sonde outages. *J. Geophy. Res.***114**: D07111, DOI: 07110.01029/02008JD010651.

Lovejoy S, Tuck SF, Schertzer D, Hovde SJ. 2009b. Reinterpreting aircraft measurements in anisotropic scaling turbulence. *Atmos. Chem. Phys.* **9**: pp. 5007–5025, DOI: 10.5194/acp-9-5007-2009.

Lovejoy S, Tuck AF, Schertzer D. 2010. The horizontal cascade structure of atmospheric fields determined from aircraft data. *J. Geophys. Res.* **115**: D13105, DOI: 10.1029/2009JD013353.

Lynch P. 2006. *The Emergence of Numerical Weather Prediction: Richardson's Dream*, Cambridge University Press: Cambridge; 18–20, DOI: 10.2277/0521857295.

Marsan D, Schertzer D, Lovejoy S. 1996. Causal space–time multifractal processes: predictability and forecasting of rain fields. *J. Geophy. Res.* **31D**: 26333–326346, DOI: 10.1029/96JD01840.

Monetti RA, Havlin S, Bunde A. 2003. Long-term persistence in the sea surface temperature fluctuations. *Physica A* **320**: 581–589, DOI: 10.1016/S0378-4371(02)01662-X.

Monin AS. 1972. *Weather Forecasting as a Problem in Physics*. MIT Press: Boston, MA; 1–13.

NCEP. 2003. *Office Note 442: The GFS Atmospheric Model*. Environmental Modeling Center. http://www.emc.ncep.noaa.gov/officenotes/newernotes/on442.pdf (accessed 6 February 2009)

Okamoto K, Derber J. 2006. Assimilation of SSM/I radiance in the NCEP global data assimilation system. *Mon. Weather Rev.* **134**: 2612–2631, DOI: 10.1175/MWR3205.1.

Palmén E. 1959. On the maintenance of kinetic energy in the atmosphere. In: *The Atmosphere and the Sea in Motion*, Bolen B (ed.). Oxford University Press: Oxford; 212–224.

Palmer TN. 2001. A nonlinear dynamical perspective on model error: a proposal for non-local stochastic-dynamic parametrization in weather and climate prediction models. *Q. J. R. Meteorol. Soc.* **127**: 279–304, DOI: 10.1002/qj.49712757202.

Palmer TN, Williams P (eds). 2010. *Stochastic Physics and Climate Models*. Cambridge University Press: Cambridge; 480 pp.

Penland C. 1996. A stochastic model of IndoPacific sea surface temperature anomalies. *Physica D* **98**: 534–558, DOI: 10.1016/0167-2789(96)00124-8.

Radkevitch A, Lovejoy S, Strawbridge KB, Schertzer D, Lilley M. 2008. Scaling turbulent atmospheric stratification, Part III: empirical study of space–time stratification of passive scalars using lidar data. *Q. J. R. Meteorol. Soc.* **134**: 317–335, DOI: 10.1002/qj.203.

Richardson LF. 1922. *Weather Prediction by Numerical Process*. Cambridge University Press. Republished by Dover, 1965.

Schertzer D, Lovejoy S. 1987. Physical modeling and analysis of rain and clouds by anisotropic scaling of multiplicative processes. *Journal of Geophysical Research* **92**: 9693–9714, DOI: 10.1029/JD092iD08p09693.

Schertzer D, Lovejoy S, Lavallée D. 1993. Generic multifractal phase transitions and self-organized criticality. In *Cellular Automata: Prospects in Astronomy and Astrophysics*. Perdang JM, Lejeune A (eds). World Scientific; 216–227.

Schertzer D, Tchigirinskaya I, Lovejoy S, Tuck A. 2012. Quasi-geostrophic turbulence and generalized scale invariance, a theoretical reply. *Atmos. Chem. Phys.* **12**: 327–336, DOI: 10.5194/acp-12-327-2012.

Sela JG. 1982. *The NMC Spectral Model*. NOAA Technical Report NWS-30, NOAA NWS: Silver Spring, MD; 30 pp.

Sela JG. 1988. The new NMC operational spectral model. In *Eighth Conference on Numerical Weather Prediction*, Baltimore, Maryland, 22–26 February.

Smith TM, Reynolds RW, Peterson TC, Lawrimore J. 2008. Improvements to NOAA's historical merged land–ocean surface temperature analysis (1880–2006). *J. Climate* **21**: 2283–2293, DOI: 10.1175/2007JCLI2100.1.

Stolle J, Lovejoy S, Schertzer D. 2009. The stochastic cascade structure of deterministic numerical models of the atmosphere. *Nonlin. Proc. Geophys.* **16**: 1–15, DOI: 10.5194/npg-16-607-2009.

Tennekes H. 1975. Eulerian and Lagrangian time microscales in isotropic turbulence. *J. Fluid. Mech*, **67**: 561–567, DOI: 10.1017/S0022112075000468.

Uppala SM, Kallberg PW, Simmons AJ, Andrae U, Da Costa Bechtold V, Fiorino M, Gibson JK, Haseler J, Hernandez A, Kelly GA, Li X, Onogi K, Sarinen S, Sokka N, Allan RP, Anderson E, Arpe K, Balmaseda MA, Beljaars ACM, Van de Berg L, Bidloti J, Bormann N, Caires S, Chevallier F, Dethof A, Dragosavac M, Fisher M, Fuentes M, Hagemann S, Holm E, Hoskins BJ, Isaksen L, Janssen PAEM, Jenne R, McNally AP, Mahfouf J-F, Morcrette J-J, Rayner NA, Saunders RW, Simon P, Sterl A, Trenberth KE, Untch A, Vasiljevic D, Viterbo P, Woollen J. 2005. The ERA40 re-analysis. *Q. J. R. Meteorol. Soc.* **131**: 2961–3012, DOI: 10.1256/qj.04.176.